



Multiple Spiral Arms in the Disk around Intermediate-mass Binary HD 34700A

John D. Monnier¹, Tim J. Harries², Jaehan Bae³, Benjamin R. Setterholm¹, Anna Laws², Alicia Aarnio⁴, Fred C. Adams^{1,5}, Sean Andrews⁶, Nuria Calvet¹, Catherine Espaillat⁷, Lee Hartmann¹, Stefan Kraus², Melissa McClure⁸, Chris Miller¹, Rebecca Oppenheimer⁹, David Wilner⁶, and Zhaohuan Zhu¹⁰

¹Astronomy Department, University of Michigan, Ann Arbor, MI 48109, USA; monnier@umich.edu

²Department of Physics and Astronomy, University of Exeter, Exeter, EX4 4QL, UK

³Department of Terrestrial Magnetism, Carnegie Institution for Science, 5241 Broad Branch Road, NW, Washington, DC 20015, USA

⁴University of Colorado Boulder, Boulder, CO 80303, USA

⁵Physics Department, University of Michigan, Ann Arbor, MI 48109, USA

⁶Harvard-Smithsonian Center for Astrophysics, Cambridge, MA 91023, USA

⁷Boston University, Boston, MA, USA

⁸European Southern Observatory, Garching, Germany

⁹American Museum of Natural History, New York, NY, USA

¹⁰University of Nevada, Las Vegas, NV, USA

Received 2018 May 11; revised 2018 December 10; accepted 2018 December 15; published 2019 February 19

Abstract

We present the first images of the transition disk around the close binary system HD 34700A in polarized scattered light using the Gemini Planet Imager instrument on Gemini South. The *J*- and *H*-band images reveal multiple spiral-arm structures outside a large ($R = 0''.49 = 175$ au) cavity, along with a bluish spiral structure inside the cavity. The cavity wall shows a strong discontinuity, and we clearly see significant non-azimuthal polarization U_ϕ , consistent with multiple scattering within a disk at an inferred inclination $\sim 42^\circ$. Radiative transfer modeling along with a new *Gaia* distance suggest HD 34700A is a young (~ 5 Myr) system consisting of two intermediate-mass ($\sim 2 M_\odot$) stars surrounded by a transitional disk and not a solar-mass binary with a debris disk, as previously classified. Conventional assumptions of the dust-to-gas ratio would rule out a gravitational instability origin to the spirals while hydrodynamical models using the known external companion or a hypothetical massive protoplanet in the cavity both have trouble reproducing the relatively large spiral-arm pitch angles ($\sim 30^\circ$) without fine-tuning of gas temperature. We explore the possibility that material surrounding a massive protoplanet could explain the rim discontinuity after also considering effects of shadowing by an inner disk. Analysis of archival *Hubble Space Telescope* data suggests the disk is rotating counterclockwise as expected from the spiral-arm structure and revealed a new low-mass companion at $6''.45$ separation. We include an appendix that sets out clear definitions of Q , U , Q_ϕ , U_ϕ , correcting some confusion and errors in the literature.

Key words: infrared: planetary systems – planetary systems – planet–disk interactions – protoplanetary disks – techniques: high angular resolution – techniques: polarimetric

Supporting material: data behind figures

1. Introduction

Planet formation relies on the interplay of several physical processes involving dust, ice, gas, chemistry, as well as the radiation field from the central star, as shadowed by inner disk structures. Observations are needed to determine the importance of effects such as gravitational instability (GI; Boss 1997), streaming instability (Johansen et al. 2007), dust growth (Birnstiel et al. 2010), core accretion (Pollack et al. 1996), planetary migration (Tanaka et al. 2002), and more. Theorists hope to eventually build a predictive framework that can explain the observed demographics of exoplanets around low- and intermediate-mass stars, but we are currently far from achieving this goal.

Fortunately, modern high angular resolution techniques have opened powerful new ways to validate physical models. For low-mass stars, mm-wave imaging (e.g., Fedele et al. 2018; Huang et al. 2018) and scattered-light coronagraphic imaging (e.g., Rapson et al. 2015; Avenhaus et al. 2018) routinely find symmetric ring structures possibly caused by accreting or still-forming protoplanets (Bae et al. 2017). For intermediate-mass ($1.5\text{--}3 M_\odot$) stars, we find more varied structures, such as asymmetric complex disks (e.g., AB Aur;

Oppenheimer et al. 2008) and spirals (e.g., MWC 758, HD 135344B, HD 142527; Garufi et al. 2017), in addition to multiple rings (e.g., HD 163296, HD 169142; Monnier et al. 2017). Avenhaus et al. (2018) pointed out that spiral structures appear mainly around intermediate-mass stars and not the lower-mass T Tauri stars. The explanation for this dichotomy is not known, but larger stars tend to have higher disk masses and higher companion fractions, both of which lead to more spiral structure.

In this work, we present the discovery of one of the most “spiral-armed” disks so far around HD 34700A, with structures reminiscent of the HD 142527 system (Avenhaus et al. 2017). HD 34700A is a close binary system (period 23.5 days) originally thought to consist of two nearly equal-mass main-sequence solar-mass stars (spectral type G0, $T_{\text{eff}} \sim 6000$ K) at 125 pc with large far-infrared excess interpreted as a “Vega-like” (debris) disk (Torres 2004). Torres (2004) anticipated that a farther distance would mean a more massive and younger system, and indeed the new *Gaia* distance now places this system at 356.5 ± 6.1 pc, nearly three times farther away than previously assumed. Assuming solar metallicity and the new distance, we find HD 34700A to consist of two $\sim 2.05 M_\odot$ stars with nearly identical effective temperatures (5900 and 5800 K)

Table 1
Target Information

Names	HD 34700A, HIP 24855	
R.A. (J2000)	05 ^h 19 ^m 41 ^s .42	Gaia Collaboration et al. (2018)
Decl. (J2000)	+05° 38' 42" 80	Gaia Collaboration et al. (2018)
<i>R</i> mag	8.80 ± 0.06	Fujii et al. (2002)
<i>J</i> mag	8.041 ± 0.023	Skrutskie et al. (2006)
<i>H</i> mag	7.706 ± 0.023	Skrutskie et al. (2006)
<i>K_s</i> mag	7.482 ± 0.024	Skrutskie et al. (2006)
Spectral Type	G0+G0	Mora et al. (2001), Torres (2004)
T_{eff}	5900 K+5800 K	Torres (2004)
Binary ^a Period (days)	23.4877 ± 0.0013	Torres (2004)
Distance (pc)	356.5 ± 6.1	Gaia Collaboration et al. (2018)

Note.

^a In addition to unresolved spectroscopic companion with period 23.5 days, Sterzik et al. (2005) noted fainter companions at 5''2 and 9''2 away.

Table 2
Observing Log of Polarimetry Observations Using Gemini Planet Imager

UT Date	Target Name	Filter	T_{int} (s)	N_{coadds}	N_{Frames} ^a	Airmass	rms Wavefront Error (nm)
2018 Jan 03	HD 34700A	<i>J</i>	29.10	2	32	1.25–1.32	206–252
2018 Jan 03	HD 34700A	<i>H</i>	29.10	2	32	1.23–1.24	201–252

Note. For these observations, we used the default occulting spot, apodizer, and Lyot stop appropriate for the observing waveband.

^a Here we refer to the number of frames used in the data reduction, where a frame consists of N_{coadds} images coadded with individual exposures times of T_{int} seconds at a single half-wave plate position.

and a system age of ~ 5 Myr (details provided in Section 4.1). We can now interpret the infrared excess as a transition disk with ongoing planet formation rather than an older, more evolved “debris” disk.

The closest known stellar companion (HD 34700B) to the inner pair of stars (HD 34700Aa, Ab) was reported by Sterzik et al. (2005) at separation of 5''18 (projected separation of 1850 au) at PA 69°1 with photometry $J = 12.29$, $H = 11.52$, and $K = 11.03$. Assuming a coeval system and that the *K*-band flux is entirely unreddened stellar flux, this suggests that the HD 34700B is a $0.7 M_{\odot}$ K7 star with $T_{\text{eff}} = 4000$ K (Siess et al. 2000). *Gaia* DR2 now includes this companion, and it seems to be at the same distance as HD 34700A. We will discuss the possibility of tidal interactions of HD 34700B with the HD 34700A disk later in this paper. Sterzik et al. (2005) report a slightly fainter fourth component at 9''2 (projected separation of 3300 au; listed but with no parallax solution yet in *Gaia* DR2), which we will not discuss further, although it could potentially also play a role in sculpting the outer disk structure of HD 34700A, depending on the true 3D orbital geometry.

After describing our new GPI observations in detail, we present a simple radiative transfer model that explains many of the observed properties of the disk, although serious deficiencies remain. Lastly, we ran hydrodynamical simulations tuned for HD 34700A and discuss the difficulty in matching the large pitch angle spirals with conventional disk prescriptions for both an outer perturber (HD 34700B) or a protoplanet in the mostly dust-free cavity. In an appendix, we clearly define the Stokes conventions adopted here, correcting some confusion found in the literature. Also in an appendix, we present a preliminary analysis of archival *HST* data, identifying a possible fifth member of this system. ALMA data will be needed in order to allow a comprehensive modeling of the HD 34700A disk and

to determine the physical origin of the extensive spiral structures.

2. Observations and Data Processing

We report new imaging of HD 34700A using the Gemini Planet Imager (GPI; Macintosh et al. 2008, 2014; Poyneer et al. 2016) installed on Gemini South. In polarimetry mode (Perrin et al. 2015) with the adaptive optics system and an occulting spot, GPI can obtain high dynamic range imaging of scattered light from *Y*–*K* bands relying on the physics of scattering to deliver a distinctive polarization pattern. Light scattered from dust grains surrounding a star will be polarized with E-field vectors aligned perpendicular to the radial direction toward the star, while the light from the central star’s point-spread function (PSF) will be typically unpolarized or linearly polarized throughout the PSF.

We observed HD 34700A on UT 2018 January 3, utilizing the standard GPI coronagraphic configurations (specifically “J-coron” and “H-coron”), including the use of a coronagraphic spot (0''184 diameter for *J* band and 0''246 diameter for *H* band) and appropriate Lyot and apodizing pupil masks. We chose ~ 30 s integration time to avoid detector saturation by light around the spot. We coadded two frames together to accumulate ~ 1 minute of on-source exposure time per file, a limit imposed by the rotating field of view in the GPI design. We used the Wollaston prism mode and rotated the half-wave plate 22°5 between four 1 minute observations to determine the Stokes parameters (half-wave plate angles 0°, 22°5, 45°, 67°5 were used). A total of 32 frames were saved for *J*- and *H*-band observations, leading to 8 independent sequences with 4 equally spaced half-wave plate angles. Table 1 contains the information on the target star, while Table 2 contains the Observing Log.

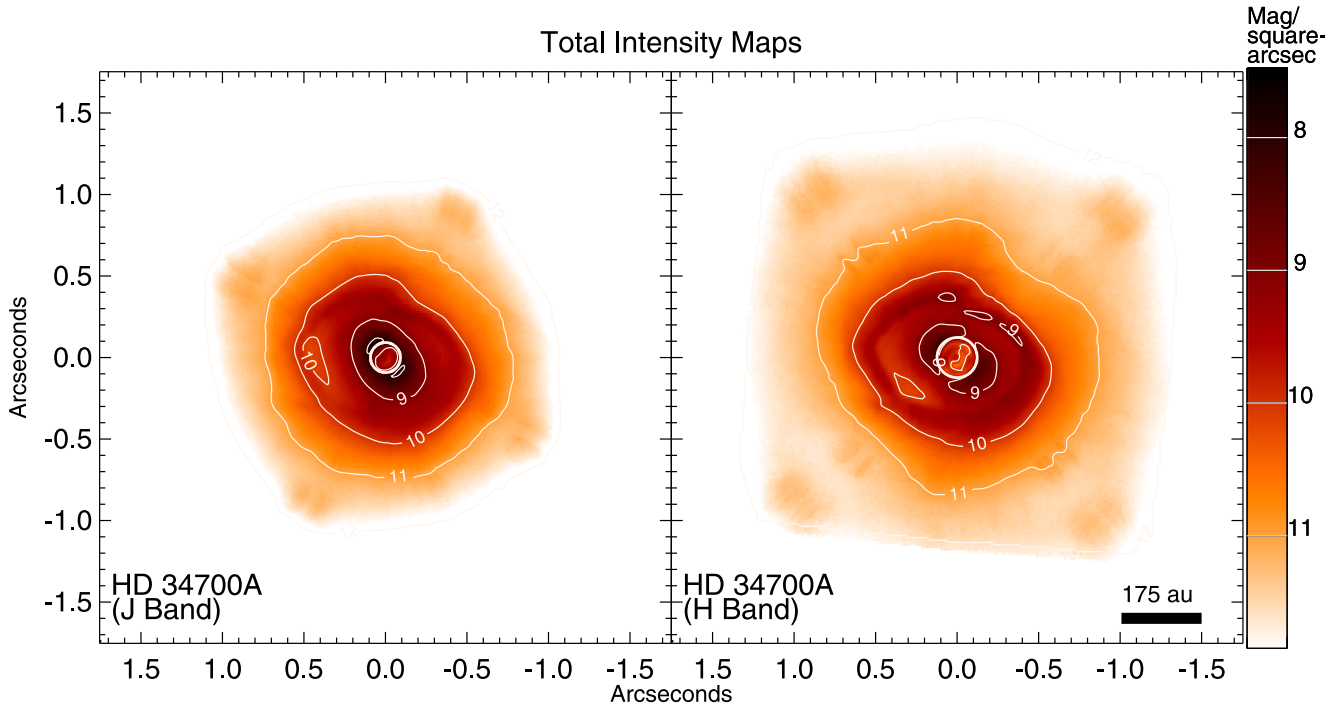


Figure 1. Total intensity maps, measured by the Gemini Planet Imager, shown using a linear color table (see color bar). The intensity scales with the local surface-brightness levels, labeled with contours in units of Vega magnitudes/square-arcsecond. The approximate location and size of the occulting spot is marked with a white circle in each panel. East is left; north is up. Note that most of the halo of light (especially within $0''.3$) is from the residual stellar point-spread function, although one can clearly see the ring-like circumstellar scattering from the HD 34700A transition disk. The data used to create this figure are available.

For this “discovery” paper, we have used only GPI pipeline primitives to simplify the data reduction description. All steps to create a flux-calibrated Stokes data cube (I , Q , U , V), including bias correction, bad-pixel corrections, flat-fielding, and flux calibration, were carried out using the IDL-based GPI pipeline version 1.4.0 (downloaded on 2018 August 06). The general calibration procedures have been described by Perrin et al. (2014) and Millar-Blanchaer et al. (2016), with a discussion of flux calibration by Hung et al. (2016).

2.1. Analysis Steps

Here we give detail on each of the major analysis steps leading to the calibrated Stokes data cubes.

Locating star position: In order to precisely determine the star’s location behind the coronagraphic spot and to calibrate the flux scale for GPI, the instrument contains a diffractive element in the pupil plane that creates so-called satellite spots. Each of these spots has a radial structure that points back toward the location of the star and contains a certain percentage of the flux from the star. The GPI pipeline centers each frame using a high-pass filter, followed by a Radon transform to find the stellar location to within ± 0.1 pixels (pixel scale 14.14 mas) using the symmetry of the diffractive spots (Wang et al. 2014). Also, by carrying out aperture photometry on these spots, one can deduce the flux from the star assuming the photometry in Table 1. The H -band spots in the polarization mode were extensively studied by Hung et al. (2016), and a $\pm 13\%$ systematic error was recommended to be used in addition to any statistical error due to variations in spot-to-star flux ratios observed during engineering studies. The J -band polarization mode has not been studied as systematically—here, we use the second-order satellite spots, which contain

$\sim 25\%$ less flux¹¹ than the first-order spots, because they are better separated from the speckle halo and adopt a 20% systematic error (R. De Rosa 2019, private communication, GPI team).

Calibrating flux. We median-combined all the total intensity images in the instrument frame before estimating photometry, and our errors combine systematic and statistical errors in quadrature. We report calibration factors in the form following Wolff et al. (2016): $1 \text{ ADU/s/coadd} = X \text{ mJy/arcsec}^2$, where X is the calibration factor. For J band we find calibration factor to be $3.7 \text{ mJy}/(\text{ADU/s})/\text{coadd}/\text{arcsec}^2 \pm 22\%$, and for H band we find $3.7 \text{ mJy}/(\text{ADU/s})/\text{coadd}/\text{arcsec}^2 \pm 15\%$ (coincidentally, they are the same number within 2 significant figures). We note that these values are only appropriate for photometry of point-source detections and cannot be strictly applied for diffuse, extended brightness distributions. Proper photometry of the diffuse component requires knowledge of the PSF, including Strehl and scale of the residual speckle halo.

Removing polarized flux from star PSF. Because of the high level of scattered light from circumstellar dust—seen even in individual frames—we used only light behind the coronagraphic spot for estimating the linear polarization of the stellar signal (i.e., Millar-Blanchaer et al. 2016). Once we have the fractional $f_{Q,U,V}$ of light behind the spot, we can multiply this by the total intensity I in each pixel throughout the PSF to estimate the Q , U , V contamination and subtract these contributions from the linear polarization. For reference, we report the mean stellar linear polarization ($P_{\text{band}} = (f_Q^2 + f_U^2)^{\frac{1}{2}}$,

¹¹ This and related GPI calibration information will be posted publicly on the Gemini Observatory website at <http://www.gemini.edu/sciops/instruments/gpi/>.

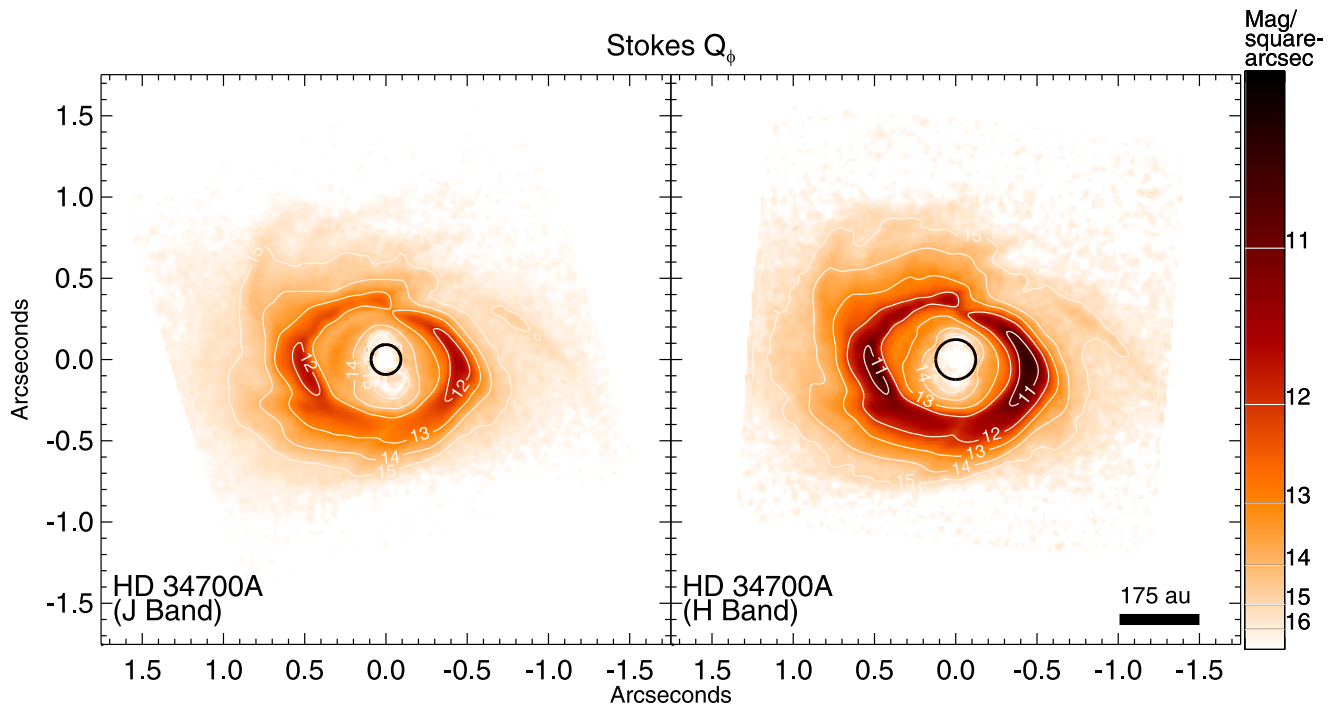


Figure 2. Q_ϕ maps, measured using the Gemini Planet Imager, shown using a color table proportional to the square-root of absolute value of azimuthal-component of polarized intensity Q_ϕ (see the text for a description of this quantity). The maps were smoothed by a flux-conserving Gaussian with FWHM 30 mas (2.1 pixels) to improve SNR. The local surface-brightness levels can be found as labeled contours in units of Vega magnitudes/square-arcsecond. The approximate location and size of the occulting spot is marked with a black circle in each panel. East is left; north is up. The data used to create this figure are available.

$\Theta = \frac{1}{2} \arctan \frac{U}{Q}$) that we removed (all angles are degrees east of north): HD 34700A $P_J = 0.61\% \pm 0.08\%$ at $\Theta = 12^\circ \pm 5^\circ$, $P_H = 0.82\% \pm 0.08\%$ at $\Theta = -17^\circ \pm 8^\circ$. The errors reported previously are based on the scatter among the eight independent Stokes data cubes (each based on 4 HWP positions) and do not include systematics. The observed stellar polarization angle Θ varied $\sim 10^\circ$ as a function of parallactic angle within each set, strongly suggesting that these measurements are partially contaminated by uncorrected instrumental effects and not purely intrinsic. We refer the reader to the GPI instrumentation papers referenced in Section 2 for more information on the systematic errors related to removal of the instrumental signature in the pipeline. That said, generally our values are broadly consistent with the small level of polarization measured in V band by previous workers. Specifically, Bhatt & Manoj (2000) reported no detectable linear polarization in V band, while Oudmaijer et al. (2001) found V -band polarization $P_V = 0.35 \pm 0.06\%$ with $\Theta \sim 28^\circ \pm 5^\circ$, consistent with interstellar origin.

Creating final Stokes data cubes. Following subtraction of the mean stellar polarization signal from the Stokes data cube (one for each group of four files), we then median-combined multiple Stokes data cubes spanning a range of parallactic angles after rotating images to be aligned with “True North.” The current pipeline determines the sky orientation based on the calibration of Konopacky et al. (2014), and the systematic error is estimated to be ± 0.13 (De Rosa et al. 2015). Lastly, we project the traditional Stokes Q , U components (oriented relative to north/east) onto a local Stokes Q_ϕ , U_ϕ based on the stellar position determined earlier in the processing. In this

procedure (see the derivation in Schmid et al. 2006; Avenhaus et al. 2014; Garufi et al. 2014; Millar-Blanchaer et al. 2016), linear polarization vectors that are perpendicular to the line connecting the star to the pixel are positive in Q_ϕ space, whereas radial polarization patterns are negative. Similarly polarization vectors oriented $\pm 45^\circ$ from this are found in the U_ϕ component. See Appendix A for more detail on the definition of Q , U , Q_ϕ , U_ϕ , as misleading descriptions are common in the literature. This local projection is very practical because single-scattering should be oriented around the stellar position and produce a purely positive Q_ϕ signal, while noise can be both positive and negative. Furthermore, miscalibrations (especially in the inner PSF halo) will produce a residual systematic U_ϕ signal that can be used to assess data quality and guard against false conclusions. That said, we find here a strong U_ϕ signal that we identify as an astrophysical signature of an inclined disk, consistent with predictions of Canovas et al. (2015) and Dong et al. (2016a), who explored polarization signatures for optically thick, more edge-on disks.

Bootstrapping errors. All error analysis in work has been based on bootstrap sampling, where we randomly sample the eight independent Stokes data cubes (with replacement) and calculate the median Stokes data cube for 100 bootstraps. From this median Stokes cube, we then calculate Q_ϕ , U_ϕ . These 100 bootstrapped synthetic data sets are available throughout the later analysis steps, allowing all derived quantities (such as radial profiles, fraction polarizations, etc.) to have their errors properly determined. While there will be systematic errors unmonitored by this, at least effects from read noise, photon noise, bias correction, and varying AO performance will be represented in the uncertainties presented here.

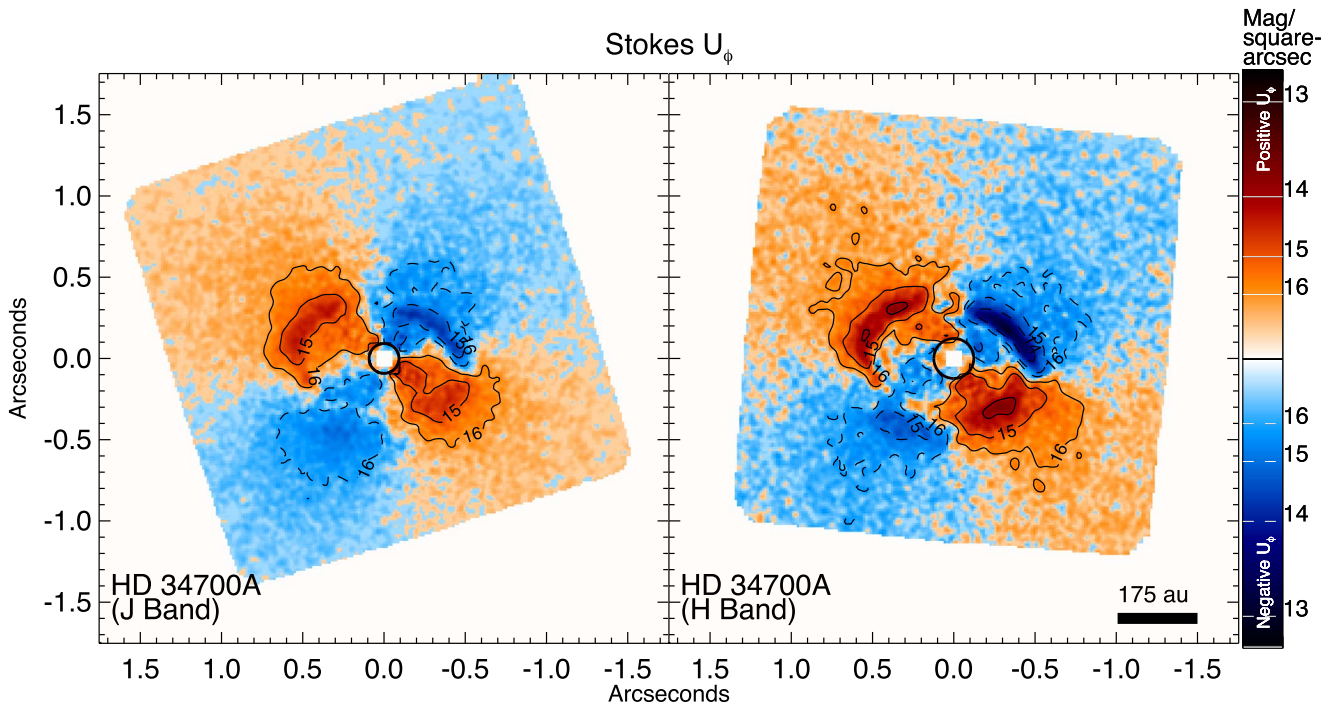


Figure 3. U_ϕ maps, measured using the Gemini Planet Imager, shown using a color table proportional to the square-root of absolute value of polarized intensity U_ϕ (see the text for a description of this quantity), where red color shows positive U_ϕ and blue color shows negative U_ϕ . The maps were smoothed by a Gaussian with FWHM 30 mas (2.1 pixels). The local surface-brightness levels can be found as labeled contours in units of Vega magnitudes/square-arcsecond. The approximate location and size of the occulting spot is marked with a black circle in each panel. East is left; north is up. The data used to create this figure are available.

2.2. Analysis Discussion

There are some additional calibration steps that are often carried out in the analysis of polarization data, most of which were expertly discussed in Avenhaus et al. (2018). Here is a brief list of calibration steps we did not include, along with the reasons behind our decision.

1. Methods that minimize U_ϕ using extra free parameters (see Avenhaus et al. 2018). When looking at very faint polarized light, it is sensible to adjust free parameters representing instrumental calibration factors to minimize the amplitude of U_ϕ , as this quantity is often intrinsically small or zero for single-scattering disks. However, in our case we have very strong scattered light for an inclined disk, and so it is not safe to assume U_ϕ is zero. It is by design that we do not attempt to minimize U_ϕ , as such procedures may remove the actual astrophysical signal.
2. Deconvolution methods. Avenhaus et al. (2018) provides an excellent demonstration of how the telescope point-spread function will convolve the observed Q , U images, which can corrupt the Q_ϕ and U_ϕ , especially too close to the star’s position or if there are sharp changes in the intensity (i.e., near strong asymmetric features). In some cases, the local polarized signal level can be reduced compared to the true value. VLT-SPHERE observers have the option of collecting a quick PSF for each observation using an ND filter, but this option is not available for GPI, and so we do not have an accurate PSF to allow for a deconvolution analysis. The best we can do is to forward convolve our modeling to see what distortions in Q_ϕ and U_ϕ might be occur—note we find none of this important for this star because the ring is

well-resolved and not located near the coronographic spot.

3. Imaging Results for HD 34700A

3.1. Basic Description

We present the total intensity maps in Figure 1, Stokes Q_ϕ maps in Figure 2, Stokes U_ϕ maps in Figure 3, and their corresponding mean radial profiles in Figure 4. Each figure has an explanation of how the images are scaled and presented. We generally present color tables that are proportional to the square-root of intensity for higher dynamic range in order to see faint details in the outer disk.

First, we discuss the total intensity maps in Figure 1. We see a depression in the center of the PSF because of the occulting mask, marked by a circle. We see the inner PSF was elongated likely due to telescope wind-shake. There are fuzzy spots outside the main PSF due to either residual “waffle mode” from the adaptive optics system or the diffractive satellite spots induced by GPI for registration of the bright star behind the coronagraph. We can clearly see the scattered light from the main dust ring here without using differential polarization; we will be able to extract a crude scattering total intensity from the dust in this ring later in this paper.

Figure 2 contains the Stokes Q_ϕ maps, showing more detail of the large dust ring, including spiral arms structures. It is useful to compare these images to the U_ϕ images in Figure 3 as residuals in the U_ϕ map often indicate the level of systematic errors in our analysis, either due to problems in the pipeline calibration or possible effects of multiple scattering for edge-on systems (as discussed by Canovas et al. 2015). Many workers

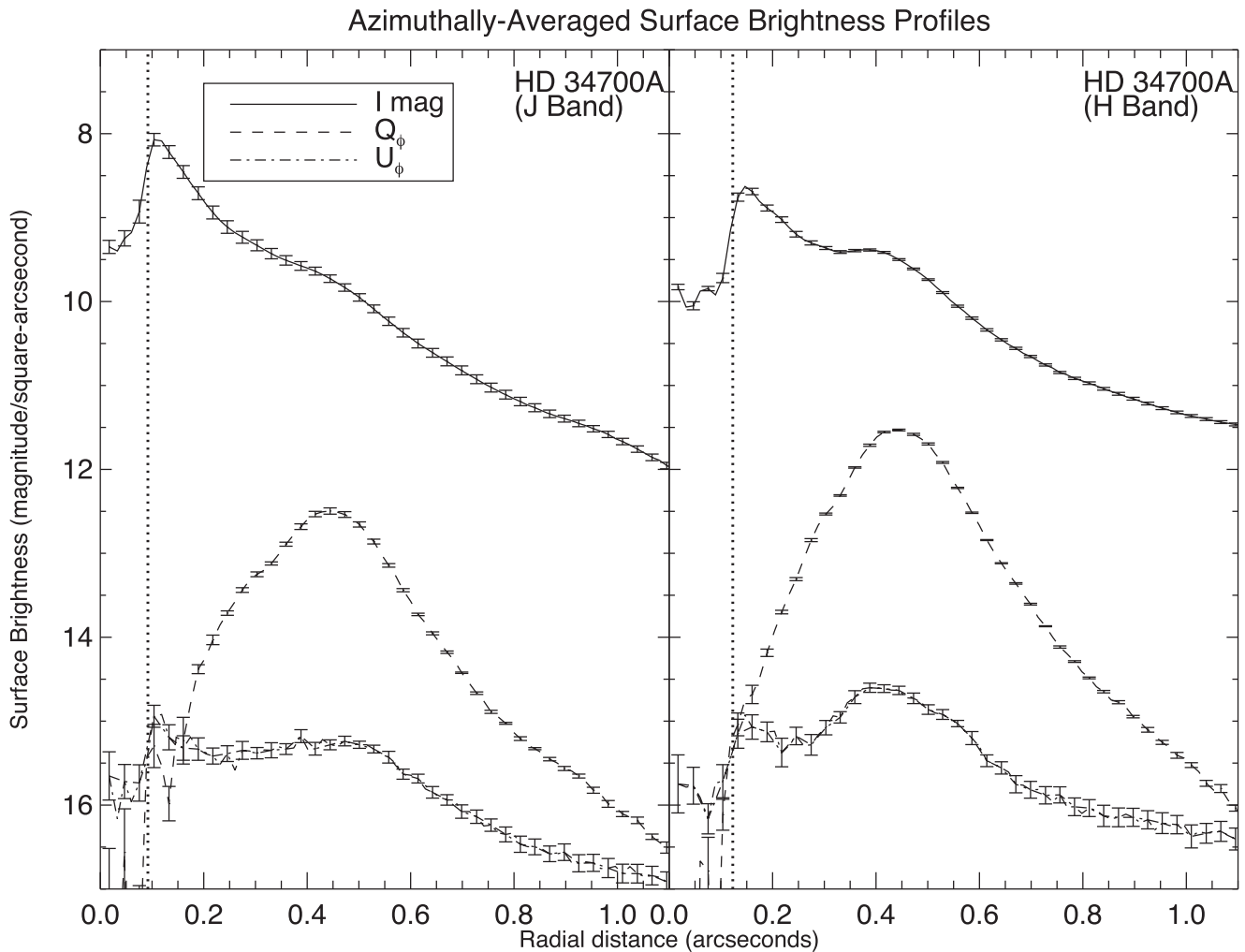


Figure 4. Azimuthally averaged surface-brightness profiles for the *J*-band and *H*-band imaging of HD 34700A are shown here. For total intensity and Q_ϕ , the surface brightnesses were averaged in annuli centered on the stellar position, then the absolute value before plotting the logarithm. For U_ϕ , the absolute value was taken first before averaging to avoid self-cancellation. The dotted vertical line shows the radius of the coronagraphic spot used. Errors were determined from bootstrap sampling of the eight independent Stokes data cubes. There is an additional overall flux calibration uncertainty (not shown) estimated to be $\pm 22\%$ at *J* band and $\pm 15\%$ at *H* band. The data used to create this figure are available.

analyzing polarization data adjust the pipeline calibration to minimize the butterfly pattern seen in U_ϕ , under the assumption there is no astrophysical signature present; this assumption should be tested for simulated disks to see if such adjustments have the possibility to erase true signal. In our case, radiative transfer modeling will support the conclusion that the bulk of our U_ϕ signal is real and not an instrumental artifact.

In order to see the faint features outside the ring, we also present an image where we have combined the *J*- and *H*-band images based on signal-to-noise ratio and labeled major features (see Figure 5). The dominant feature is an elliptical ring with a major axis diameter of $\sim 1''.0$. The ring marks the outer edge of a lower-density cavity and the beginning of the outer dust disk, as supported later in this paper by radiative transfer modeling. This ring has a marked discontinuity to the north, showing a sudden change in radius. The ring is brightest in polarized intensity to the east and west, while the total intensity appears brightest to the north. We note this is similar to the ring brightening in Q_ϕ seen in the HD 163296 (MWC 275) disk recently observed by Garufi et al. (2014) and Monnier et al. (2017), but different from the general pattern

seen in T Tauri stars where the nearside of the tilted disk is brightest in polarized light (Avenhaus et al. 2018).

Based on the brighter north side and the shift of slight off-center location of the ellipse (see the next section for more detail on ellipse fitting), we expect the north side of the disk to be tilted toward us while the south side of the disk is tilted away from us. While our flux calibration carries large photometric uncertainties, we report the total polarized flux at *J* band amounts to $\sim 1.5\%$ of the total *J*-band flux, and the polarized flux at *H* band amounts to $\sim 2.5\%$ of the total *H*-band flux.

The cavity inside this ring is not devoid of scattered light, and one sees an inner arc to the east that is more prominent at *J* band than at *H* band. We also marked the most extended spiral arm as “Arc 1,” which extends from $0''.5$ to the north out to $1''.55$ to the west. There is a group of roughly four arcs to the north and northeast, and hints of additional arc segments to the south and southeast. We estimate the pitch angle (angle between arc and circle tangent) of Arc 1 to be $\sim 20^\circ$ at $1''.5$, while the closer arcs to the northeast have a pitch angle $\sim 30^\circ$ at $0''.75$.

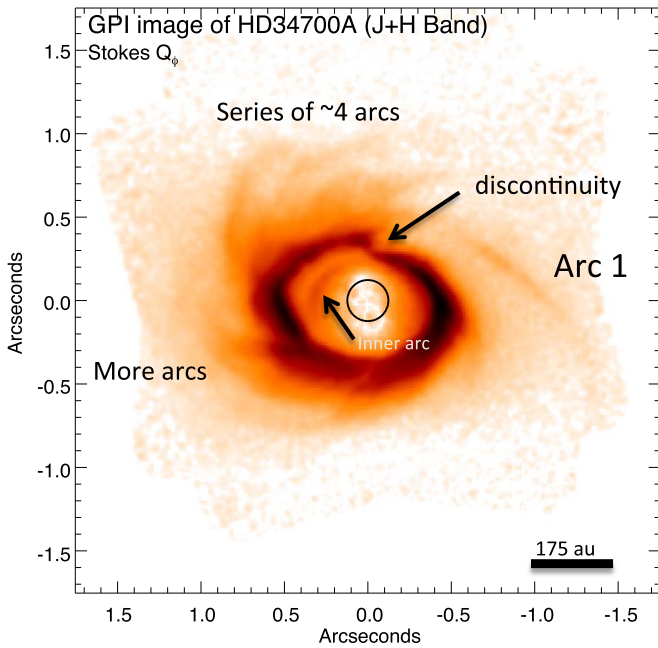


Figure 5. Combined J -band and H -band Q_ϕ maps shown using a color table proportional to the square-root of absolute value of polarized intensity Q_ϕ . The maps were smoothed by a Gaussian with FWHM 30 mas (2.1 pixels) to improve SNR and to highlight low surface-brightness features outside the main ring. The approximate location and size of the occulting spot is marked with a black circle. East is left; north is up. Features marked here are discussed in the text.

In the next section, we will analyze these features more quantitatively before carrying out radiative transfer modeling on a physical model.

3.2. Analysis of HD 34700A Ring and Spiral Structures

In Figure 6 we define some regions of the image for further analysis. We first fitted an ellipse to the ridge structure around the Q_ϕ ring seen in the combined $J + H$ image of Figure 5. We constrained the center of the ring to lie along the minor axis direction, as expected for dust scattering off the surface of a flared disk and which has been seen in other disks such as MWC 275 (Monnier et al. 2017) and many T Tauri disks (Avenhaus et al. 2018). The fitting procedure was as follows: (1) Starting from the peak in the Q_ϕ map, we followed the local maximum of the ring in both the clockwise and counter-clockwise directions. (2) These (x, y) points were fitted to an ellipse using the “least orthogonal distance” method as implemented in the MPFITELLIPSE routine from the IDL MPFIT library maintained by Craig Markwardt.¹² We expect the uncertainty in the final parameters to be dominated by irregular structures in the ring and not the pixel-based noise, such as photon noise or variations in imaging quality. To account for this, we compiled the list of (x, y) points along the ring, pruned the list to avoid spatial correlations between neighboring points induced by the PSF, then we bootstrap-sampled these points and re-fit for an ellipse many times. The values reported as follows include errors from this procedure.

From this fit, we estimate a major axis of $R = 0''.492 \pm 0''.012 = 175 \pm 5$ au inclined at $41.5 \pm 2.3^\circ$ with elongation oriented along PA $69.0 \pm 2.3^\circ$ east of north. The center of this

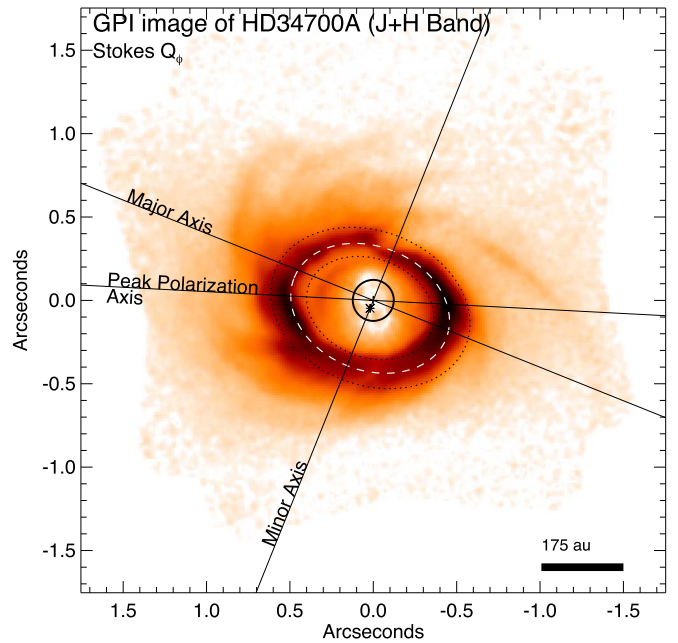


Figure 6. Geometric analysis of the HD 34700A circumstellar dust ring. We mark the axes used for radial and annular regions used in profiles cuts in later figures. We fitted an ellipse to the bright ring, shown here as a dashed line. From this fit, we estimate a major axis of $R = 0''.49 = 175$ au inclined at 42° , with elongation oriented along PA 69° east of north. The center of this ellipse (marked by asterisk) is shifted by $0''.05$ south of the measured location of the central unresolved binary.

ellipse is shifted south by $0''.051 \pm 0''.006$ from the measured location of the central unresolved binary. These features including the major and minor axis are marked in Figure 6 and will be used for creating radial plots. In addition, an annular region within $\pm 25\%$ of the best-fit ellipse has been marked and will be used for azimuth profiles.

The peak of the Q_ϕ does not lie along the major axis of this ellipse. Originally we thought this was due to dust density or wall height variations around this somewhat-irregular ring. However, radiative transfer modeling suggests that the peak polarization is more diagnostic of the true position angle of the inclined disk. We mark the angle of peak polarization on this figure as well and note this angle agrees better with the position angle separating positive/negative U_ϕ regions in Figure 3.

In Figure 7 we show the radial profiles along the three axes defined in Figure 6 of the Q_ϕ surface brightness at J and H bands. One can see the flux from the “inner arc” appearing at $0''.3$ along the major axis, showing relatively larger flux levels ($>50\%$) at J band than H band compared to the rest of the ring. The errors were calculated by bootstrap sampling of the eight independent Stokes data cubes.

Next we want to analyze the intensity around the dominant ring, identified as the inner wall of the dusty transition disk. For this particular source, we were able to extract a crude estimate of the actual total intensity of the circumstellar dust scattering by subtracting a model of the instrument PSF, something not normally possible to do with GPI data. Specifically, a Moffat function was used to approximate the PSF by fitting the total intensity image with the annular ring masked out. We used the MPFIT2DPEAK function in the IDL MPFIT library (also maintained by Craig Markwardt), defining our Moffat function as $I(x, y) = A_0 + A_1(u + 1)^{-A_2}$, where $u = ((x' - A_4)/A_2)^2 + ((y' - A_5)/A_3)^2$ and (x', y') is a reference

¹² <https://www.physics.wisc.edu/craigm/idl/fitting.html>

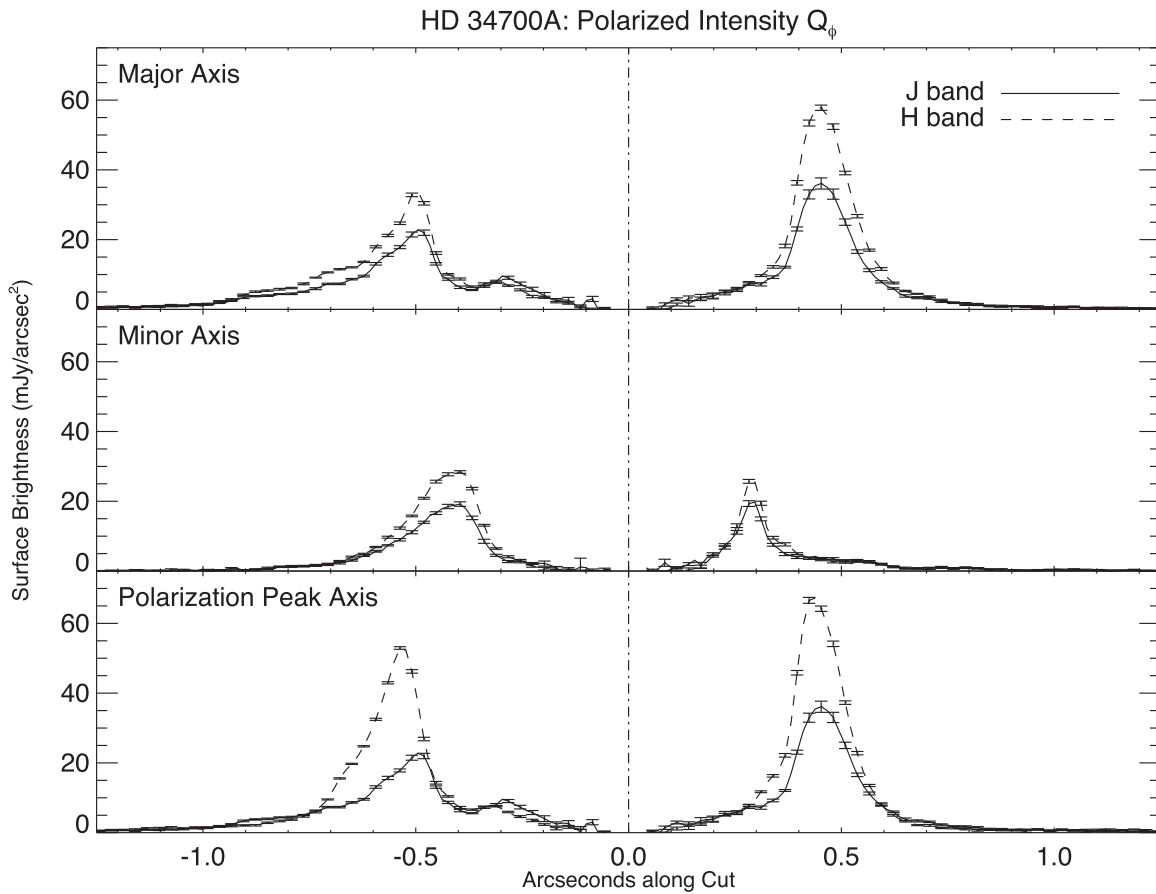


Figure 7. Here we show the radial surface-brightness profiles along the 3 axes defined in Figure 6. The surface brightness was averaged over a aperture $0''.1$ wide. Errors bars represent the rms variation in the bootstrap sampling of the eight independent Stokes data cubes in our observations. The data used to create this figure are available.

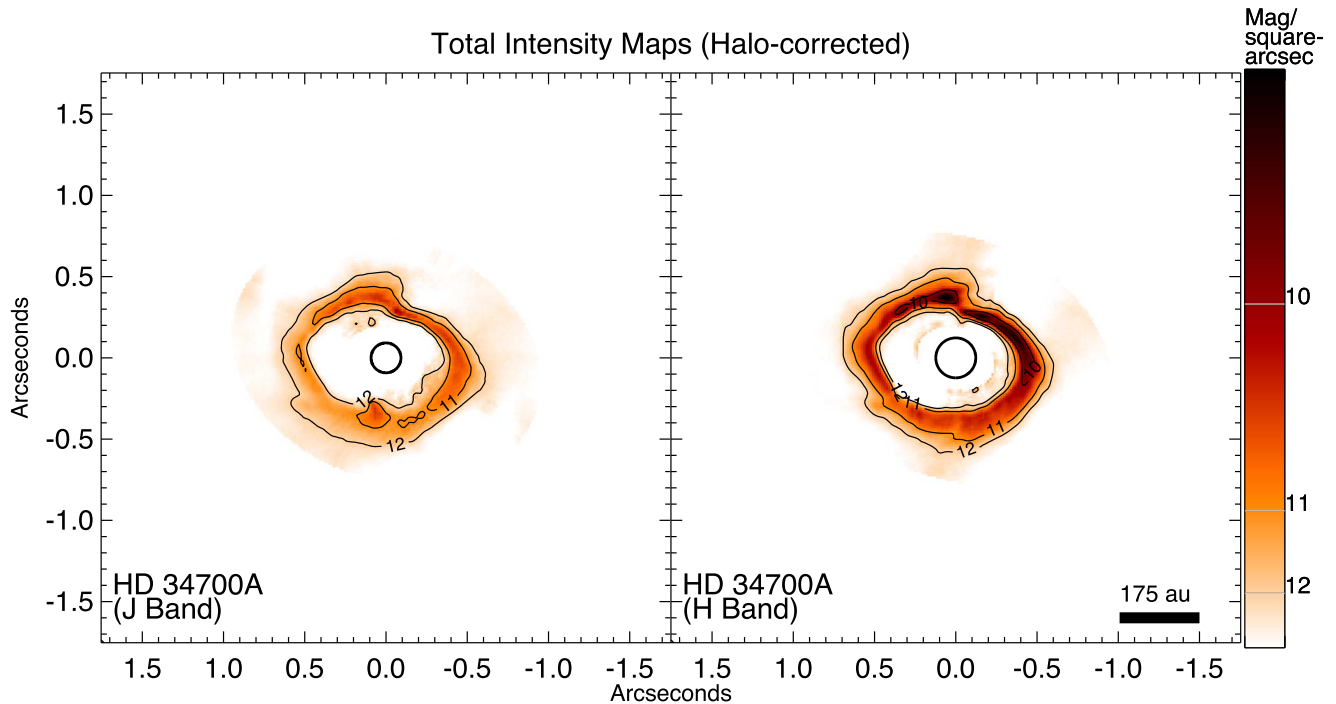


Figure 8. Total intensity of the scattered light around HD 34700A, extracted by subtracting a Moffat PSF model for the halo surrounding the coronagraphic spot. The surface brightness is shown with a linear color table. The subtraction is only valid within $\pm 30\%$ of the ring itself. The data used to create this figure are available.

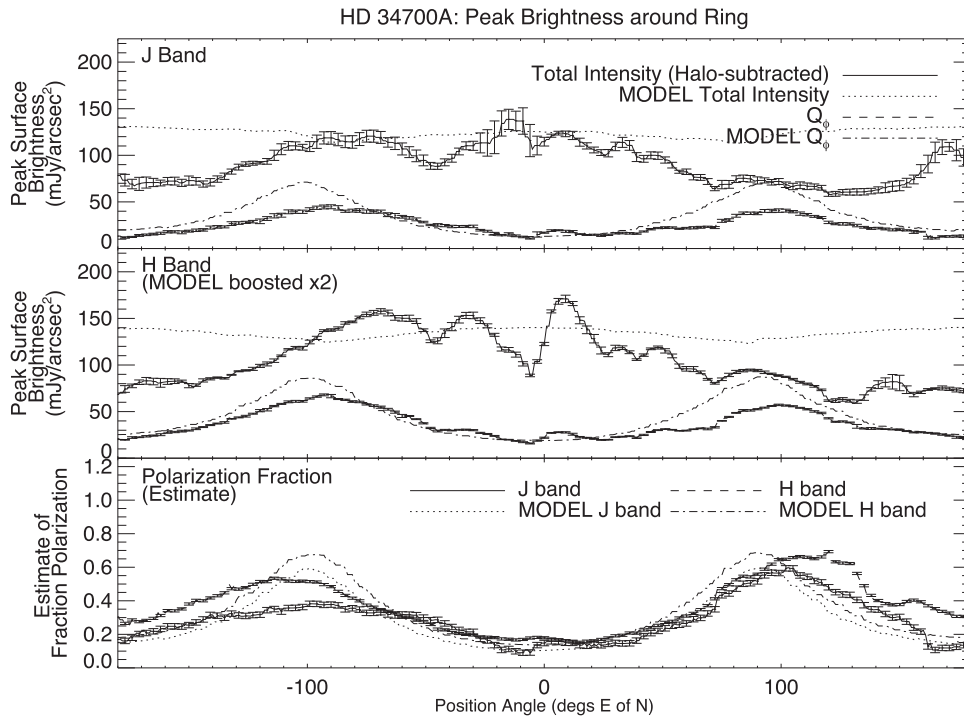


Figure 9. Total scattering intensity along with the Q_ϕ intensity as a function of azimuth around the strong circumstellar dust ring: (top) J -band results, (middle) H -band results, (bottom) estimate of the fractional polarization. We see that most scattering comes from the north, identified as the nearside of the disk, while the highest fractional polarization is on the east/west sides of the ellipse. Results from our radiative transfer model are also presented and reproduce the fraction of polarization and azimuthal variations of Q_ϕ . The H -band model intensities are systematically lower than our observed values, and we have multiplied the model H -band intensities by 2 to ease comparison with our H -band flux levels. The data used to create this figure are available.

frame tilted by angle A_6 . We restricted the fitting region to just within two annuli positioned inside and outside the best-fit ellipse that defines the ring (specifically, region 1 was between 0.4 and $0.7\times$ the ring, and region 2 was between 1.35 and $2.5\times$ the ellipse). This allows us to approximate the power-law point-source function and extract the extra scattered light coming from the ring region clearly seen in Q_ϕ (see Figure 8). For completeness, we include the Moffat function parameters we adopted for the J - and H -band total intensity extraction, along with errors based on the bootstrap sampling of the eight independent Stokes data cubes: $A_J = (-1.7 \times 10^{-5} \pm 0.2 \times 10^{-5}, 0.019 \pm 0.005, 0''.010 \pm 0''.003, 0''.008 \pm 0''.002, 0''.014 \pm 0''.018, 0''.012 \pm 0''.018, 37.5 \pm 4.0$ E of N, 0.654 ± 0.020); $A_H = (-2.5 \times 10^{-5} \pm 0.4 \times 10^{-5}, 0.0036 \pm 0.0007, 0''.021 \pm 0''.005, 0''.016 \pm 0''.004, -0''.013 \pm 0''.002, -0''.007 \pm 0''.002, 50.9 \pm 1.3$ E of N, 0.526 ± 0.024).

With the estimate of the scattered light total intensity shown in Figure 8, we can calculate the true fractional polarization, not just Q_ϕ . As part of this analysis, we searched for point sources within the halo and noted two symmetrical spots in the J -band image at radius $0''.3$ and position angle $-12^\circ/168^\circ$ (slightly evident in Figure 8). These spots appear right on the main ring but do not appear in the H -band total intensity images. Given the symmetry of the spots and the lack of H -band detection, we identify these features as adaptive optics artifacts (i.e., not physical companions such as exoplanets).

Armed with the halo-subtracted total intensity of the scattered-light disk, we constructed Figure 9, where the peak Q_ϕ surface brightness around the ring is plotted as a function of position angle within the annulus defined in Figure 6. Note we

used the Q_ϕ peak locations and found the corresponding total intensity at that location for the other observables found in Figure 9. We see the peak total intensity varies by about 50% around the ring, while the Q_ϕ varies by nearly a factor of three. The absolute fractional polarization peaks at about 50% for J band and at about 60% at H band. Figure 10 contains similar profiles around the ellipse for U_ϕ , also associated with locations where Q_ϕ is maximum at each position angle. We see the fractional U_ϕ polarization varies $\pm 3\%$ around the ring.

As part of our analysis of HD 34700A, we analyzed archival *Hubble Space Telescope* imagery from 1998. The results are interesting, though preliminary, and we have included details in Appendix B. In short, we find some evidence that the scattered light ring has rotated 5.75 ± 0.25 (error bar not including possibly large systematic errors) counterclockwise over the 19.3 years since the *HST* data was taken—the spiral arms winding is consistent with counterclockwise motion. This rotation implies an orbital period of 1200 ± 50 yr, consistent with the expected 1160 yr period for material at 175 au around the central binary with a combined mass of $4M_\odot$. We also tentatively identified a candidate brown dwarf at $6''.45$ distance (projected 2300 au), but confirmation of common proper motion has yet to be made. If confirmed, HD 34700ABCD would be a rare young quintuplet system that seems highly unstable from a dynamical point of view.

We will discuss possible origins of the marked discontinuity on the north side of the ring in later sections, including the possibility of shadowing affects from an inner disk (see Section 4) or from material around a vigorously accreting protoplanet (see Section 5).

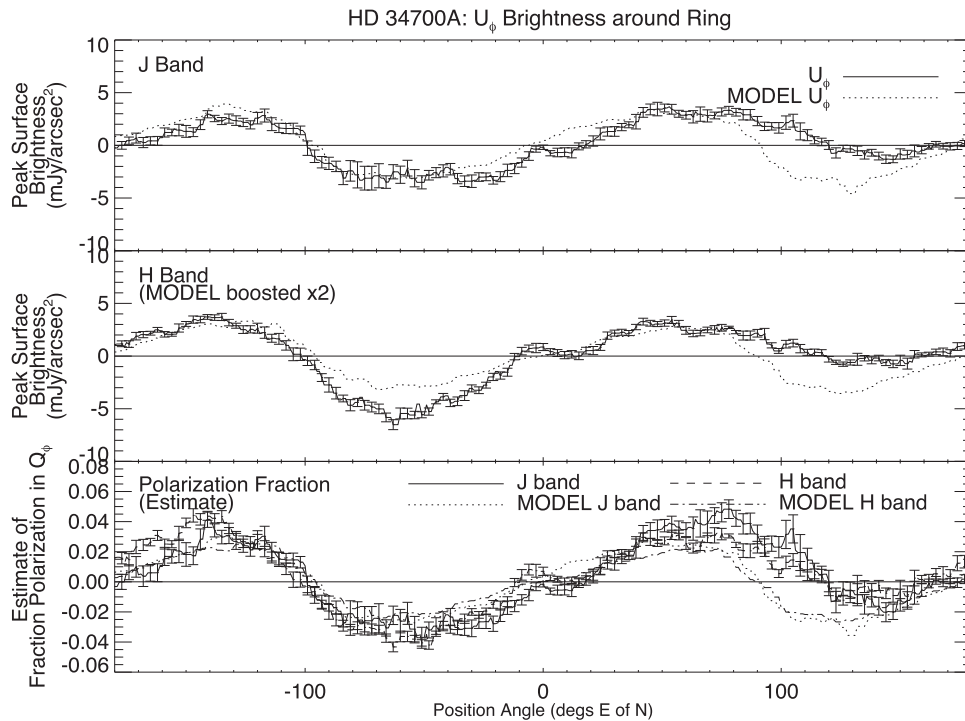


Figure 10. Total scattering intensity along with the U_ϕ intensity as a function of azimuth around the strong circumstellar dust ring: (top) J -band results, (middle) H -band results, (bottom) estimate of the fractional polarization. We see strong U_ϕ modulation as a function of position angle. The radiative transfer model presented in Section 4 reproduces this feature, and we have included the model results in the figure as well. The H -band model intensities are systematically lower than our observed values, and we have multiplied the model H -band intensities by 2 to ease comparison with our H -band flux levels. The data used to create this figure are available.

Next, we develop a radiative transfer model and will compare the model results to the observed profiles we just discussed.

4. Radiative Transfer Modeling of the HD 34700A System

Here we focus on creating a physical model for HD 34700A that can simultaneously explain the bright polarized ring and spectral energy distribution using a self-consistent two-dimensional radiative transfer calculation; future work will address the complex spiral structures and possible shadowing effects when additional data are available. Since we know a priori that our model will not fit the data well in detail, we chose to manually adjust our model parameters to achieve a qualitatively good fit to both the imaging and the SED, while constraining as many free parameters as possible to their canonical values. We estimate the errors on each of our derived parameters by calculating the range of models (fixing the other parameter) that give an equally good quantitative fit.

The modeling was conducted using the TORUS radiative transfer code (Harries 2000; Harries et al. 2004; Harries 2011), which uses the Monte Carlo (MC) radiative equilibrium method of Lucy (1999) implemented on an adaptive mesh. The TORUS code has been extensively benchmarked against analytical solutions and 1D and 2D test problems (Harries et al. 2004; Pinte et al. 2009).

The photometric data compilation of Seok & Li (2015) was adopted in this study (see their Table 1 for details). This comprises *EXPORT* *UBVRI* photometry (Mendigutía et al. 2012) plus 2MASS, *WISE*, *AKARI*, *IRAS*, and *SCUBA* data culled from online catalogs.

4.1. Stellar Parameters

The new *Gaia* distance of 356.5 pc is nearly $3\times$ farther away than expected by the spectroscopic analysis of Torres (2004) and demands a re-evaluation. We have updated the masses and ages for HD 34700A binary as follows: (1) We start with $T_{\text{eff}} = 5900$ K, 5800 K and V mag = 9.85, 9.95 (directly from Torres 2004). (2) We convert apparent magnitude to absolute magnitude using the new distance, yielding $M_V = 2.09$, 2.20. (3) Assuming solar metallicity and using the pre-main-sequence tracks of Siess et al. (2000),¹³ we find HD 34700A to be a young system (~ 5 Myr) consisting of two $\sim 2.05 M_\odot$ stars with a transition disk.

Fixing the stellar temperatures and luminosity ratio ($l_2/l_1 = 0.9$) based on the arguments provided previously, we can determine the stellar radii by fitting Kurucz model atmospheres to the optical/near-IR photometry, fixing the distance at 356 pc, and allowing the extinction (A_V) to vary while fixing the total-to-selective extinction to its canonical Milky Way value ($R = 3.1$).

A fit using *UBVRI*, *JHK*, and *WISE* 3.4 and 4.6 μm fluxes gives $R_1 = 3.80 R_\odot$, $R_2 = 3.73 R_\odot$, and $A_V = 0.2$, although the fit is rather poor (reduced chi-squared $\chi^2 = 166$). Restricting the photometry to just *UBVRI* and *JHK* gives a vastly improved fit ($\chi^2 = 18$) with $R_1 = 3.46 R_\odot$, $R_2 = 3.40 R_\odot$, and $A_V = 0$, strongly indicative of a disk excess longwards of 3.4 μm . We therefore adopted stellar radii of $R_1 = 3.46 R_\odot$, $R_2 = 3.40 R_\odot$, and zero reddening for our radiative transfer models.

¹³ Using web interface at <http://www.astro.ulb.ac.be/~siess/pmwiki/pmwiki.php?n=WWWTools.HRDfind%5D>.

Table 3
Model Parameters for HD 34700A

Parameter	Value	Description
Stellar parameters		
Primary stellar radius, R_1	3.46 R_\odot	Fitted from photometry
Secondary stellar radius, R_2	3.40 R_\odot	Linked to R_2 via luminosity ratio
Primary effective temperature	5900 K	Fixed; Torres (2004)
Secondary effective temperature	5800 K	Fixed; Torres (2004)
Stellar masses, M_*	2 M_\odot	Torres (2004)
Distance	356 pc	Gaia Collaboration et al. (2018)
A_V	0	Fitted from photometry
Orientation parameters		
Inclination, i	43°	Fixed from ellipse fit
PA of max. polarization	86°	Fixed from polarization fit
Disk parameters		
Disk dust mass, M_{disk}	$1.2(\pm 0.2) \times 10^{-4} M_\odot$	Fitted via SED
Disk flaring index, β	1.125	Fixed at canonical value
Radial density index, α	-2.125	Fixed at canonical value
Inner disk radius, R_i	175 au	Fixed from imaging measurement
Scale height at inner radius, h_i	17 ± 2 au	No PAH/VSG model. Fitted from SED
Scale height at inner radius, h_i	9 ± 2 au	PAH/VSG model. Fitted from SED
Outer disk radius, R_o	500 au	Fixed from image measurement
Grain properties, small grains		
Grain type	Silicates	Draine & Lee (1984)
Grain size, a_{small}	0.1 μm	Fixed. Required from imaging
Fraction of dust mass	0.5	Fixed
Grain properties, large grains		
Grain type	Silicates	Draine & Lee (1984)
Min grain size, a_{min}	1 μm	Fixed. Required to fit SED
Max grain size, a_{max}	1000 μm	Fixed. Required to fit SED
Grain size power-law index	-3.5	Fixed; Mathis et al. (1977)
Fraction of dust mass	0.5	Fixed

4.2. The Disk Structure

The disk density in cylindrical coordinates (r, z) is given by

$$\rho(r, z) = \rho_m \left(\frac{R_i}{r} \right)^\alpha \exp\left(-\frac{z^2}{2h(r)^2} \right), \quad (1)$$

where ρ_m is the midplane density at the inside edge of the transition disk at radius R_i , α is the density power-law index, and the scale height $h(r)$ is given by

$$h(r) = h_i (r/R_i)^\beta, \quad (2)$$

where h_i is the scale height at R_i and β is the flaring index. The value of ρ_m is found from

$$M_{\text{disk}} = \int_{R_i}^{R_o} \int_{-\infty}^{\infty} 2\pi r \rho(r, z) dz dr, \quad (3)$$

where R_o is outer disk radius. We assume that R_o marks a sharp cutoff to the outer disk.

4.3. Modeling Procedure

The disk structure was discretized on an adaptive cylindrical mesh, initially defined so that the disk was sampled vertically such that there were at least three cells per scale height at all radii. This initial grid was then further adaptively refined so that sharp opacity gradients (such as the disk inner edge) were adequately resolved, a step which is essential to capture the temperature gradients and produce the correct SED

(particularly in the near-to-mid infrared). This was achieved by iteratively refining those optically thick cells ($\tau > 1$) that neighbored optically thin cells ($\tau < 0.1$) and resulted in a mesh composed of approximately 250,000 cells.

The radiative equilibrium procedure started with 1 million photon packets for the first iteration, with the number of photon packets doubling at each iteration until the emissivity of the dust integrated across the entire volume converges to a tolerance of 1% (indicating the temperatures are well converged). This typically takes five iterations. The SEDs and images are then computed for a particular inclination using 10 million photon packets.

4.4. Modeling Strategy and the Best-fit Model

The outer disk radius (R_o) is poorly constrained by SED fitting. However, we note that ‘‘Arc 1,’’ marked in Figure 5, extends to a radius of $1''.5$, corresponding to a linear radius of ~ 500 au, so we adopted this value as our outer disk radius. The inside edge of the transition disk is defined as the radius of the bright ring ($0''.5$ or 175 au), as measured directly from the polarization images. We also fixed the inclination and position angle of the disk from the ellipse fitting results (see Section 3.2).

The brightening of the ring to the east and west in polarized light (see Figures 2 and 9) is due to scattering by grains that have polarizability that peaks at scattering angles close to 90° . Although it is possible to achieve this type of polarization

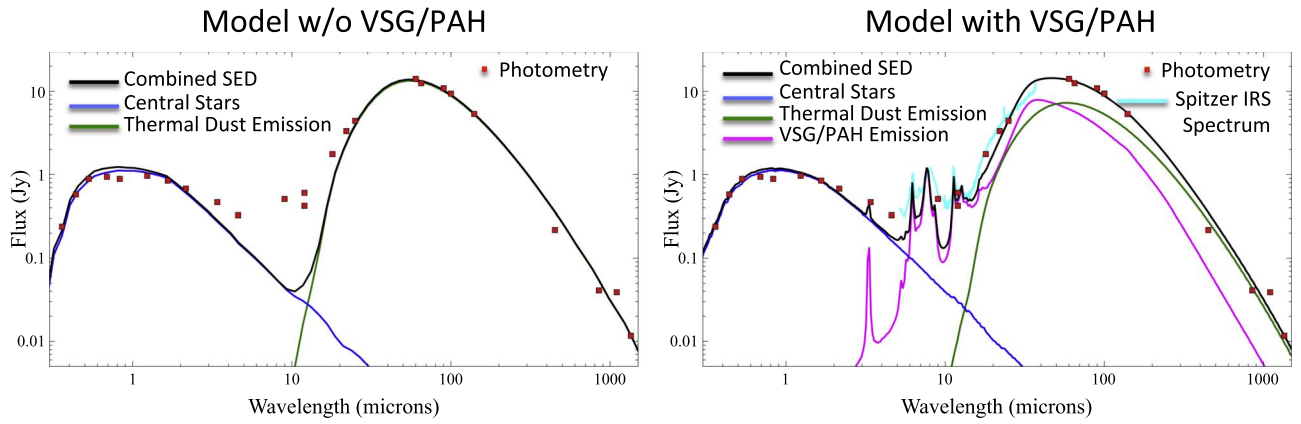


Figure 11. Radiative transfer models of HD 34700A compared with photometric observations. The left-hand panel shows the model without VSG/PAH emission and includes the direct photospheric radiation from the central star (blue line), the thermal dust emission (green line), the total SED (black line), the photometric points (red squares). The model that includes VSG/PAH emission is shown in the right-hand panel. The meaning of the colors is the same as the left-hand panel, and the contribution to the SED of VSG/PAH emission is shown (pink line) along with the *Spitzer* IRS spectrum (cyan line).

behavior with dust distributions that incorporate larger ($>1 \mu\text{m}$) grains, the forward-scattering nature of such dust leads to a significant excess of polarized light in the front part of the ring, and a corresponding deficit to the rear. We therefore include a component of small ($0.1 \mu\text{m}$) silicate grains in the model, which effectively scatter in the Rayleigh limit. However, we find that a contribution of larger grains is necessary to simultaneously fit the SED and the imaging, and we include a second distribution of dust with sizes between 1 and $1000 \mu\text{m}$ with an MRN power-law distribution (Mathis et al. 1977). We assume a dust ratio of 50:50 small grains to large grains by mass, since this is not particularly well constrained by the modeling. However the *total* mass of dust is quite well constrained by the long wavelength part of the SED.

It can clearly be seen from Figure 6 that the maximum polarization axis is offset from the major axis of the ellipse fit. Such an offset might occur if the bright inner edge of the disk was not truly circular (e.g., if it was formed from a pair of tightly wound spiral arms). We therefore investigated whether the polarization variation around the ring could give a more reliable measure of the inclination and position angle of the disk inner edge. If we assume the Rayleigh scattering phase matrix is applicable, and assume a thin ring illuminated by an unpolarized central source that scatters just once, the polarized flux P around the ring should vary as

$$P(\theta) = \gamma \sin^2 \theta, \quad (4)$$

where θ is the scattering angle and γ is a constant scaling factor that depends on the intensity of the source. The angle θ is related to the azimuthal angle (ϕ) around the ring as

$$\cos(\theta) = \cos(\phi - \delta) \sin i, \quad (5)$$

where i is the inclination and δ is the position angle of minimum polarization. We fitted the above equations to the J -band Q_ϕ curve given in Figure 9 using a χ^2 grid search, and the best fit ($\chi^2 = 3.3$) was found with $i = 43^\circ$, $\gamma = 51$, and $\delta = 4^\circ$. Hence the geometry of the ring determined from the polarization distribution gives a similar inclination to the elliptical fit but a position angle of the major axis that is significantly closer to east–west.

We fixed the power-law flaring index of the disk (β) to its canonical value of 1.125 (Kenyon & Hartmann 1987) and the

radial density power-law index (α) to -2.125 , which fixes the radial surface density power-law index to -1 . A more flared disk (i.e., a higher β) gives a polarized surface-brightness profile that is marginally shallower than the observations. With other parameters fixed, the peak of the IR thermal emission in the SED is controlled by the scale height of the inner disk. We find a value of 17 ± 2 au matches the SED, giving an h/r of the disk at 175 au of 0.1.

It has previously been established that a contribution from very small grains (VSGs) and polycyclic aromatic hydrocarbons (PAHs) is required to fit the mid-IR spectrum of HD 34700A (Seok & Li 2015). We have implemented the microphysics associated with VSG/PAH emission according to the prescription of Robitaille 2011, which in turn is a modification of the method of Wood et al. (2008). For this model, we kept the same silicate dust composition as the previous best-fit solution, but reduced the scale height of the inner edge to 9 ± 2 au in order to compensate for the additional IR emission from VSGs. The final parameters of the model presented here can be found in Table 3. We find reasonable agreement with the *Spitzer* IRS spectrum, but we are still underestimating the flux at 3.6 and $4.5 \mu\text{m}$. The Seok & Li (2015) SED fit showed a similar deficit, although the stellar parameters they used indicate they overestimated the near-IR, and thus their model mid-IR flux was higher than ours.

Note that we make no strong claims about the uniqueness of our model parameters, particularly for those whose leverage derives primarily from the SED. In fact, previous modelers have demonstrated adequate SED fits when the object was thought to be a Vega-like debris disk system at 55 pc with a 50 au cavity and a geometrically and optically thin power-law density distribution (Sylvester et al. 1996). Fortunately the *Gaia* DR2 distance has settled the largest ambiguity in the modeling, indicating that the system is a pre-main-sequence binary with a transitional disk and providing a much tighter constraint on the total dust mass. In combination with the distance, we also possess new constraints from our imaging data, in particular the location of the disk inner edge and the surface-brightness profile in scattered light (which constrains the disk flaring). The scale height of the inner edge is then determined by both the mid-IR peak of the SED, and by the polarized surface brightness of the imaging (see Section 4.5).

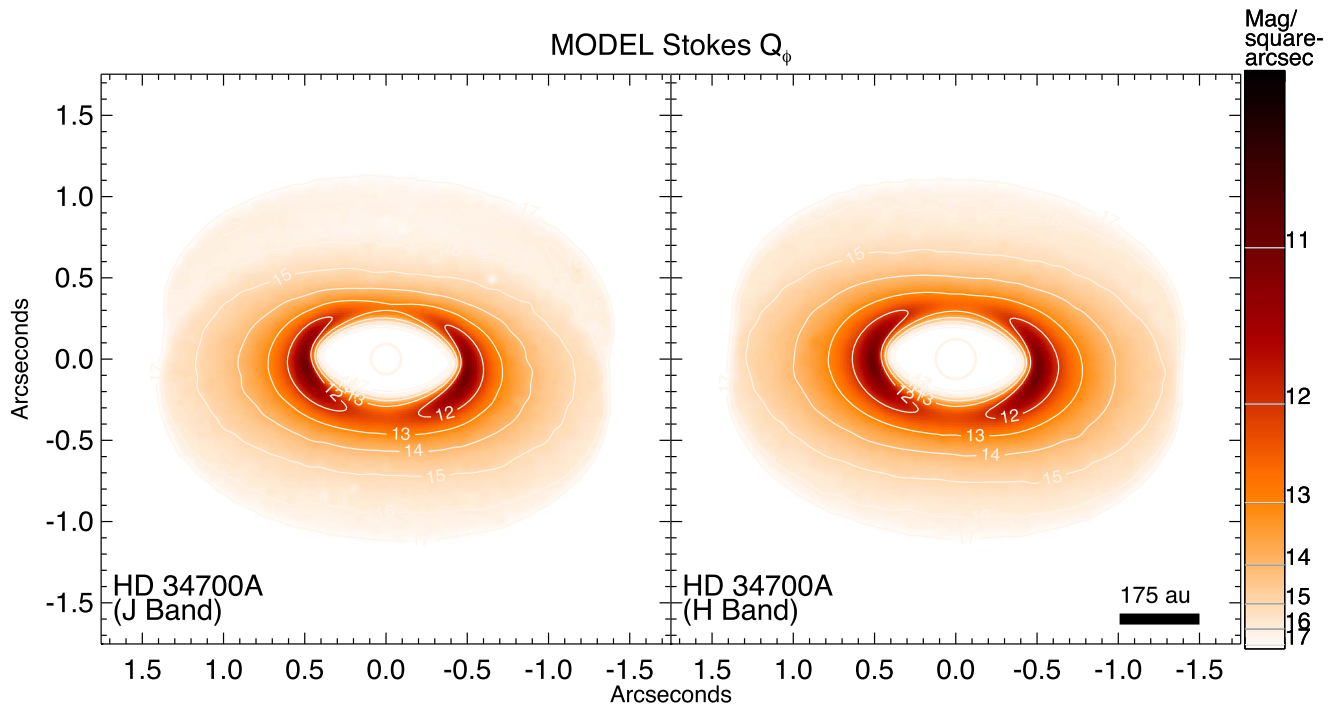


Figure 12. Simulated Q_ϕ images of HD 34700A in *J* band and *H* band based on the radiative transfer model w/o VSG/PAH described in the text, smoothed to the same angular resolution as our data. The model captures the basic shape and location of the ring, including the east–west brightening. The data used to create this figure are available.

4.5. Comparison of Models to Data

Figure 11 shows the results of the model SED compared to the collected photometry. We see that VSG/PAH emission is needed to explain the emission between 3 and 20 μm . For comparing to GPI data, we only show results for the model w/o VSG/PAH for simplicity, since both models give similar results for the *J* and *H* band. Figure 12 shows the azimuthal-component of the polarized intensity Q_ϕ for the model w/o VSG/PAH, reproducing the strong east–west brightening along the main ring. More impressive might be Figure 13, which shows the model U_ϕ surface brightness has the same butterfly pattern seen in the real U_ϕ data in Figure 3—confirming the pattern predicted by Canovas et al. (2015).

We can be more quantitative in our comparison of the model and GPI images—we have included the model intensities for Q_ϕ and U_ϕ in Figures 9 and 10. Here we see excellent agreement at *J* band (where the model was optimized) with good Q_ϕ and U_ϕ agreement, although the total intensity varies less azimuthally in these models than in our data. The overall model *H*-band intensities are $2\times$ smaller than the observed fluxes, and we have boosted them in these figures to make the comparison to data easier. Note that our photometric calibration of both *J* and *H* bands are poor, and thus we cannot rule out calibration errors in explaining this $\times 2$ discrepancy. The fractional polarization for both *J* and *H* bands does not depend on absolute photometric calibration, and we see that the model polarization fraction is a bit higher than we observe.

More exploration of the disk parameters should improve agreement between models and data. Qualitatively, we suggest that higher model *H* flux, more forward scattering on the front side of disk, and lower fractional polarization could be achieved with larger grains or varying dust constituents (e.g., ice mantles, carbon grains).

Another weakness of our current model is the adoption of a dust-free cavity, which of course cannot produce the scattered light in the low-density cavity seen in our images, although one must account for the wings of the telescope/adaptive optic system PSF to determine the true intrinsic polarized flux just inside the rim.

In fact, the reduced chi-squared values of our best-fit stellar atmosphere indicate that the optical/near-IR photometric data are formally inconsistent with pure stellar emission, even when fitting the *UBVRI* data alone. Furthermore, our RT models undershoot the *WISE* photometry (see Figure 11), even when PAH/VSG emission is included. (We note that the fits by Seok & Li 2015 demonstrate a similar behavior.)

If one were to adopt a marginally lower stellar luminosity (thus degrading the fit to the optical photometry), one could conclude there was an near-IR excess, and thus evidence for an unresolved warm (~ 1500 K) disk component very close to central binary. This putative inner disk would then cast shadows on the outer disk (an observation which in itself means that any inner disk cannot be too flared, or the ring at 175 au would be much fainter). Of course, the inner disk might not necessarily be aligned with the outer disk, and the misalignment could contrive to produce the inner arc (see Figure 5), for example. However, a misaligned inner disk should cast diametrically opposed shadows on the bright ring (e.g., Benisty et al. 2017), which are not observed. We defer a three-dimensional RT study of this system to a future paper.

5. Possible Interpretation of Disk Features and Hydrodynamic Models

While our radiative modeling allows us to explain the general appearance of HD 34700A in terms of the dust density and temperature distributions, the specific features like the

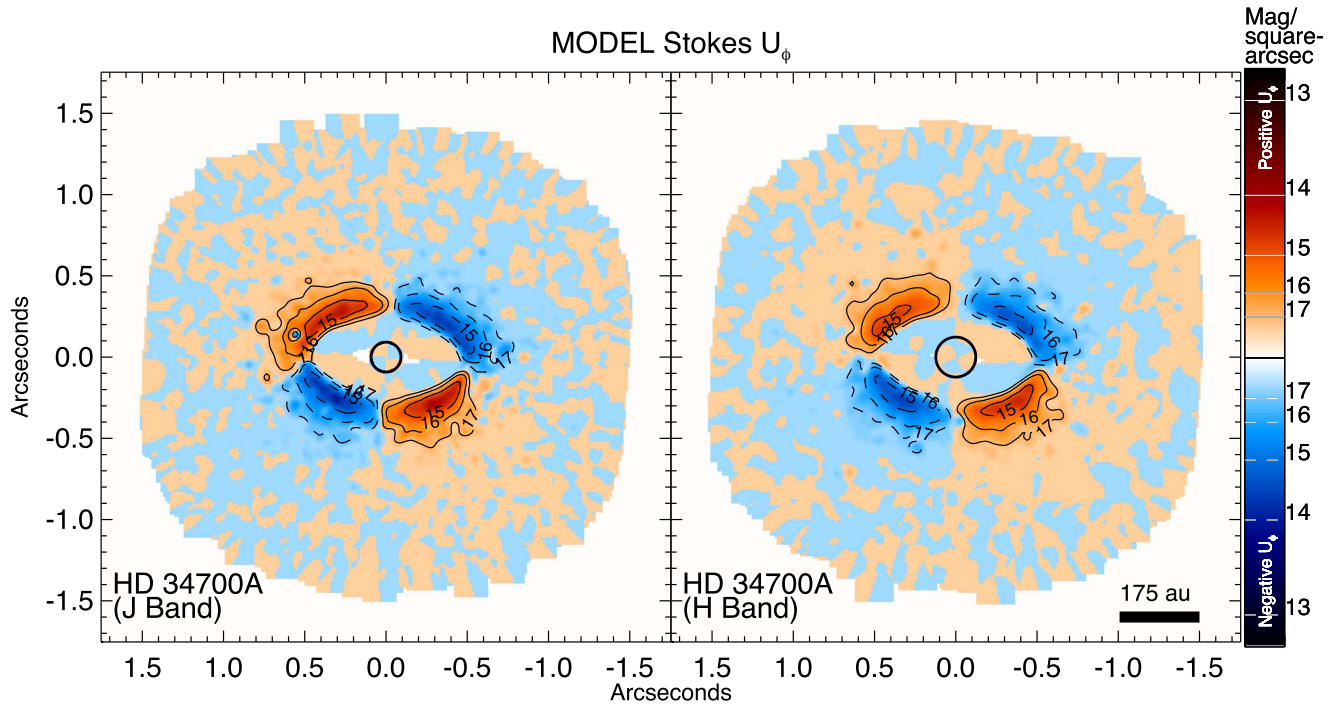


Figure 13. Simulated U_ϕ images of HD 34700A in *J* band and *H* band based on the radiative transfer model w/o VSG/PAH described in the text, smoothed to the same angular resolution as our data. The radiative transfer modeling naturally produces the “butterfly” pattern seen in our data (see Figure 3), supporting the claim that the observed U_ϕ to be from multiple scatterings in an optically thick disk, and not due to miscalibrations or systematic errors in the pipeline. The data used to create this figure are available.

spiral arms and the discontinuities seen in Figure 5 require a hydrodynamics approach. Indeed, most of the features seen in the HD 34700A transition disk must have their origin in disk hydrodynamics. We briefly discuss relevant processes:

1. *Binary system at the center (HD 34700Aa,Ab).* It has been recently suggested that the observed structures in the HD 142527 disk, including inner cavity and spirals (Avenhaus et al. 2017), can be explained by the interaction between the disk and the binary companion at the center of the system (Price et al. 2018). The semimajor axis of the binary assumed in the models of Price et al. (2018) is a significant fraction of the cavity size (26.5–51.3 au versus ~ 100 au). Other numerical simulations of circumbinary disks also show that the size of the inner cavity opened by the central binary is a factor of a few larger than the binary semimajor axis (e.g., Pierens & Nelson 2018). However, in case of HD 34700A the cavity size (~ 175 au) is orders of magnitude larger than the semimajor axis of the central binary (0.69 au), making this possibility unlikely to be the main origin of the cavity and spirals.
2. *Unseen planetary companion(s) within the inner cavity.* Having a sufficiently massive planetary companion in the cavity will naturally explain the cavity. Regarding spiral arms, two-dimensional hydrodynamic simulations show that companion with a circular orbit can launch only one or two spiral arms exterior to its orbit (Bae & Zhu 2018a), because the constructive interference among wave modes to form spiral arms becomes unavailable far from the companion (Bae & Zhu 2018b). It is therefore unlikely that a single companion having a circular orbit excites all

the observed spiral arms. When a companion has an eccentric orbit, however, it will introduce additional families of wave modes having different orbital frequency (Goldreich & Tremaine 1980). These waves can constructively interfere with each other, forming a larger number of spiral arms than a companion with a circular orbit. If the set of spiral arms in the northeastern side of the disk (noted with “series of ~ 4 arms” in Figure 5) are driven by one unseen planetary companion within the inner cavity, for instance, it is very likely that the object has an eccentric orbit. Alternatively, multiple planetary companions within the inner cavity can be the cause of the large number of spiral arms in the disk.

3. *External companion (HD 34700B).* It is possible that the external companion HD 34700B excites spiral arms in the disk around the central binary. Numerical simulations showed that a companion star in a binary system can excite spiral arms in the disk around the primary star (e.g., HD 100453; Dong et al. 2016b). However, in case of a stellar companion whose mass is a significant fraction of the primary star (in this case primary binary), the companion generates nearly axisymmetric, $m = 2$ spiral arms (Fung & Dong 2015; Bae & Zhu 2018a). The external companion is therefore not sufficient to explain all the observed spiral arms. With the *Gaia* DR2, the distances to HD 34700A and HD 34700B are the same within parallax errors, consistent with HD 34700B being gravitationally bound with HD 34700A. Since the true three-dimensional distance between the systems is likely larger than the projected distance of 1850 au, it is unlikely that HD 34700B is responsible for exciting the spiral arms. The same holds true for HD 34700C or

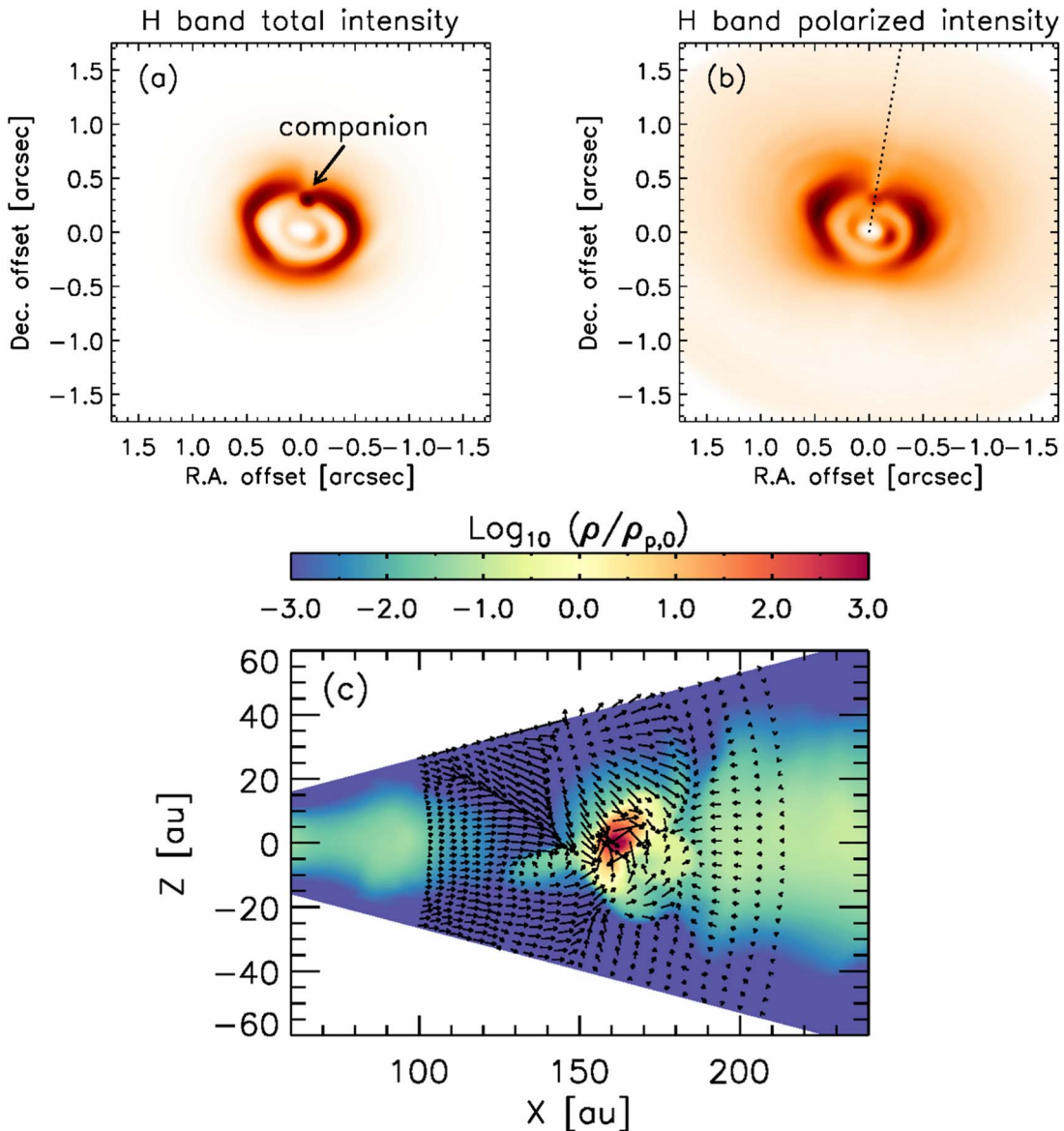


Figure 14. Simulated (a) total and (b) polarized intensity maps of HD 34700A in H band based on the hydrodynamical simulation described in Section 5. The images are smoothed to the same angular resolution as our data. We use a linear color table for the total intensity map and a color table proportional to the square-root of absolute value for the polarized intensity map, consistent with Figures 1 and 2. This model included a planet responsible for carving out the inner cavity and for producing a discontinuity in the ring due to shadowing for the outer disk inner wall by the flows surrounding the planet. Panel (c) presents the disk density distribution along the dotted line crossing the planet’s location in panel (b). The density is normalized by its initial value at the location of the planet. The overplotted arrows present the gas velocity field on the two-dimensional plane, showing complex gas dynamics around the planet. We note that this simulation did not produce the prominent high-pitch-angle spiral arcs seen in the observed images, although some tightly wound outer spiral arms were generated.

HD 34700D, which are at an even larger projected distance and without *Gaia* parallax yet to confirm physical association.

4. *Gravitational instability.* Based on the disk surface density and temperature profiles obtained with the radiative transfer modeling presented in Section 4, the Toomre Q parameter is greater than 25 everywhere in the disk with 100:1 gas-to-dust mass ratio. The disk is therefore unlikely to be gravitationally unstable currently.

In order to examine the potential origin of the disk features, we carried out three-dimensional hydrodynamic simulations. In particular, we examined whether an unseen planetary companion in the inner cavity could be responsible for the observed

disk structures using FARGO 3D (Masset 2000; Benítez-Llambay & Masset 2016) to simulate disk hydrodynamics. The hydrodynamic simulation domain covered 54 to 810 au ($0''.15$ to $2''.25$) in the radial direction, 15° above and below the midplane in the meridional direction, and the entire 2π in the azimuthal direction. We used the disk density and temperature profiles described in Section 4.2 to initialize our simulation. We used an isothermal equation of state, and the disk temperature was assumed to be vertically isothermal. We adopted 256 logarithmically spaced radial grid cells, 288 uniformly spaced azimuthal grid cells, and 80 uniformly spaced meridional grid cells. A constant α viscosity of 3×10^{-3} was applied. We used outflow boundary condition at the radial and meridional

boundaries. We ran hydrodynamic simulations for 50 companion orbits, varying companion mass, semimajor axis, and orbital eccentricity.

We then generated simulated scattered-light images by post-processing hydrodynamic models using a radiative transfer code, RADMC3D version 0.41.¹⁴ We used the same spherical mesh of the hydrodynamic simulations for radiative transfer calculations. To produce stellar photons, we placed two $2 M_{\odot}$ stars with $3.3 R_{\odot}$ and $T_{\text{eff}} = 5900$ K and 5800 K, as constrained above for HD 34700Aa and HD 34700Ab. For simplicity, we placed both stars at the center of the system. We first calculated the dust temperature with a thermal Monte Carlo simulation using 10^8 photon packages. We then computed full polarized scattering off dust particles, using the PA and inclination of the disk obtained in Section 3.2.

Figure 14 shows simulated total and polarized intensity maps in H band for a $50 M_J$ planet with semimajor axis of 135 au and orbital eccentricity of 0.2. The planet clears the inner disk and generates a ring-like structure beyond its orbit. In this model, the violent three-dimensional gas flows around the planet block stellar photons, casting shadows on the ring beyond the planet’s location. This is possible because the gas flows around the planet have a comparable vertical extent to the inner disk and a larger density. As a result, this shadow produces a feature similar to the observed discontinuity in total and polarized maps. We found that the vertical extent and the density of the circumplanetary flows are dependent on planet mass and orbital eccentricity, and that we need both large planet mass and non-zero eccentricity to reproduce the observed discontinuity (Appendix C). We do, however, caution that our hydrodynamic model may not have a sufficient numerical resolution and proper thermodynamics to accurately simulate the circumplanetary flows. Future numerical simulations will further test the possibility of circumplanetary flows casting shadows onto the outer disk, and better constrain the mass and orbital eccentricity of the hypothetical planet.

In our hydrodynamic simulations, planets with non-zero orbital eccentricity excite multiple spiral arms in the outer disk. However, these spirals are too tightly wound compared with the observed ones and produce insufficiently strong perturbations, so they are not apparent when the raw images are smoothed to the same angular resolution as the data. As the pitch angle of and density perturbations driven by spiral arms depend sensitively on both radial and vertical disk thermal structure (Zhu et al. 2015; Juhász & Rosotti 2018), future numerical simulations with proper treatments for disk thermodynamics, including heating from spiral shocks, stellar irradiation, and vertical thermal stratification of the disk, will help us better understand the origin of the spiral arms in the disk. From the observational side, better constraints on the disk temperature profile using molecular line emissions will help us further examine the possible causes of the spirals in the disk.

In general, the inner stellar binary, the planetary orbit, and the disk could all be in somewhat different planes. Such inclination angle differences could generate additional dynamics, and these interactions should also be explored in future calculations. Also, given that 50 Jupiter-mass planets/brown dwarfs are rare, we recognize that shadows casted by circumplanetary flows may not be commonly seen.

Lastly, we comment generally on how to interpret the shallow, 20° – 30° pitch angles observed for the spiral arcs in HD 34700A. Numerical simulations of GI in protoplanetary disks show that the pitch angles are typically 10° to 20° (Cossins et al. 2009; Dong et al. 2015; Forgan et al. 2018). One interesting feature seen in GI simulations is that GI-driven spirals have a constant pitch angle (of course within the same simulation), although why they do so has not yet been understood (Forgan et al. 2018). For companion-driven spirals, pitch angles vary significantly as a function of radius, from $\sim 90^{\circ}$ at the vicinity of the companion to almost zero degrees far from the companion (see Figure 6 of Zhu et al. 2015 and Figure 5 of Bae & Zhu 2018b). In the case of HD 34700B driving the observed spirals, the location where spirals are observed is $\sim 10\%$ of the distance to HD 34700B (150 versus 1500 au). For such a situation, the pitch angle is expected to be $< \sim 10^{\circ}$, although a warm surface can make spirals more opened in scattered light images (e.g., Benisty et al. 2015).

6. Conclusions

We have presented discovery images of the remarkable disk around HD 34700A, including a large low-density cavity about $1'' = 360$ au across. We see signs of possible ongoing planet formation, including a discontinuous ring and a rich series of spiral arcs (possibly up to 8 arcs). With the new *Gaia* distance, we can better identify this system as a young ~ 5 Myr intermediate-mass binary system ($2M_{\odot} + 2M_{\odot}$) with a very prominent transition disk, and not an older debris disk system as previously classified.

Our image analysis and radiative transfer modeling suggest this system is inclined about 42° , with the north side tilted toward us. The butterfly pattern in the U_{ϕ} suggests multiple scattering within the disk, and this interpretation is supported by our radiative transfer modeling. This pattern can be a powerful diagnostic of the true geometry of the disk inclination when the disk ring emission is not truly circular. For inclined optically thick disks, we caution against using pipeline procedures that aggressively attempt to remove the U_{ϕ} signal as a calibration shortcut, without further study of the effect on true U_{ϕ} signals using simulated data.

The brightening of the polarized intensity along the major axis of the ring is reminiscent of the Herbig Ae star HD 163296 (MWC 275) disk observed by Garufi et al. (2014) and Monnier et al. (2017), but unlike the T Tauri disks of Avenhaus et al. (2018), which all show bright Q_{ϕ} on the nearside of the disk, not the edges. This may mark another difference between Herbig and T Tauri disks, or perhaps it is due to the differences between dust populations that exist at a cavity wall compared to dust existing in the upper layers of a flared disk.

While the known close inner binary cannot explain the large transition disk cavity, an inner perturber (i.e., forming exoplanet) can explain the large lower-density hole in the disk as well as some of the inner wall discontinuity. We found that a sufficiently massive protoplanet could cause local shadowing of the outer disk, reminiscent of the ring “discontinuity” we observe for HD 34700A, although shadowing by an inner circumbinary or circumstellar disk could also play a role (as for HD 142527; Avenhaus et al. 2017). That said, the hydrodynamical simulations predict spiral arms much more tightly wound than observed. Since companion-driven spiral arms are increasingly tightly wound as they propagate (Zhu et al. 2015; Bae & Zhu 2018a), it is difficult to reconcile the observed large

¹⁴ <http://www.ita.uni-heidelberg.de/~dullemond/software/radmc-3d/>

pitch angle with the external companion HD 34700B, unless the disk temperature is largely increased (at least at the surface), as suggested for other disks with spirals (e.g., Benisty et al. 2015). Thus, we still lack a definite cause for the multiple spiral arcs for this source in particular and for intermediate-mass stars in general (à la Avenhaus et al. 2018).

Future observations should focus on high angular resolution ALMA gas and dust continuum imaging to continue probing the origin of the spiral structures seen often in intermediate-mass disks. Also, new visible and near-infrared scattered light imaging with better attention to the absolute photometric calibration will enable next-generation radiative transfer modeling to tightly constrain the dust properties. Lastly, a search for point sources within the disk might reveal the inner planet responsible for the large cavity seen in the HD 34700A transition disk.

J.D.M/A.A. acknowledge support from NSF AST 12100972, 1311698, 1445935, and 1830728. A.A. also acknowledges support from the CU Boulder Hale Fellowship program. The RT calculations presented in this paper were performed on the University of Exeter Supercomputer, a DiRAC Facility jointly funded by STFC, the Large Facilities Capital Fund of BIS, and the University of Exeter, and on the DiRAC Complexity system, operated by the University of Leicester IT Services, which forms part of the STFC DiRAC HPC Facility (www.dirac.ac.uk). The latter equipment is funded by BIS National E-Infrastructure capital grant ST/K000373/1 and STFC DiRAC Operations grant ST/K0003259/1. T.J.H. acknowledges funding from Exeter’s STFC Consolidated Grant (ST/J001627/1). S.K. acknowledges support from an STFC Rutherford Fellowship (ST/J004030/1) and a European Research Council (ERC) Starting Grant (Grant agreement No. 639889). J.B. acknowledges support from NASA grant NNX17AE31G and computational resources and services provided by the NASA High-End Computing Program through the NASA Advanced Supercomputing Division at Ames Research Center.

This work has made use of data from the European Space Agency (ESA) mission *Gaia* (Gaia Collaboration et al. 2018) (<https://www.cosmos.esa.int/gaia>), processed by the *Gaia* Data Processing and Analysis Consortium (DPAC, <https://www.cosmos.esa.int/web/gaia/dpac/consortium>). Funding for the DPAC has been provided by national institutions, in

particular the institutions participating in the *Gaia* Multilateral Agreement.

This research has also made use of the SIMBAD database (Wenger et al. 2000), operated at CDS, Strasbourg, France, and NASA’s Astrophysics Data System Bibliographic Services.

The data presented here were obtained at the Gemini Observatory (programs GS-2017B-LLP-12), which is operated by the Association of Universities for Research in Astronomy Inc., under a cooperative agreement with the NSF on behalf of the Gemini partnership: the National Science Foundation (United States), the National Research Council (Canada), CONICYT (Chile), Ministerio de Ciencia, Tecnología e Innovación Productiva (Argentina), and Ministério da Ciência, Tecnologia e Inovação (Brazil). This work is based on observations made with the NASA/ESA *Hubble Space Telescope*, obtained from the data archive at the Space Telescope Science Institute. STScI is operated by the Association of Universities for Research in Astronomy, Inc. under NASA contract NAS 5-26555.

Lastly, we appreciate feedback from the anonymous referee that led to a more comprehensive and complete article.

Facility: Gemini:South (GPI), *HST* (NICMOS).

Software: IDL, TORUS, FARGO 3D, RADMC3D, GPI Data Reduction Pipeline,¹⁵ MPFIT.¹⁶

Appendix A

Definition of Stokes Q , U , Q_ϕ , U_ϕ

We report here for completeness the definition of Stokes Q , U and Q_ϕ , U_ϕ used in this work. Figure 15 unambiguously defines our conventions.

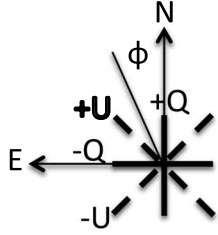
We have based our convention for Q , U position angles on the IAU standard (IAU 1974) as summarized by Hamaker & Bregman (1996). We have based the definition of Q_ϕ , U_ϕ on a modified version of the Q_r , U_r system, as first proposed by Schmid et al. (2006). The Schmid definition results in a positive Q_r value for radially polarized sources, which is not desired for observations of scattered-light disks. We note that many workers have incorrectly referred to Schmid et al. (2006) as the source for their Q , U , Q_ϕ , U_ϕ convention, but have actually adopted slightly different formulas (e.g., Canovas et al. 2015; Avenhaus et al. 2018).

In summary, the Stokes parameters defined in Figure 15 have the following properties which make them attractive:

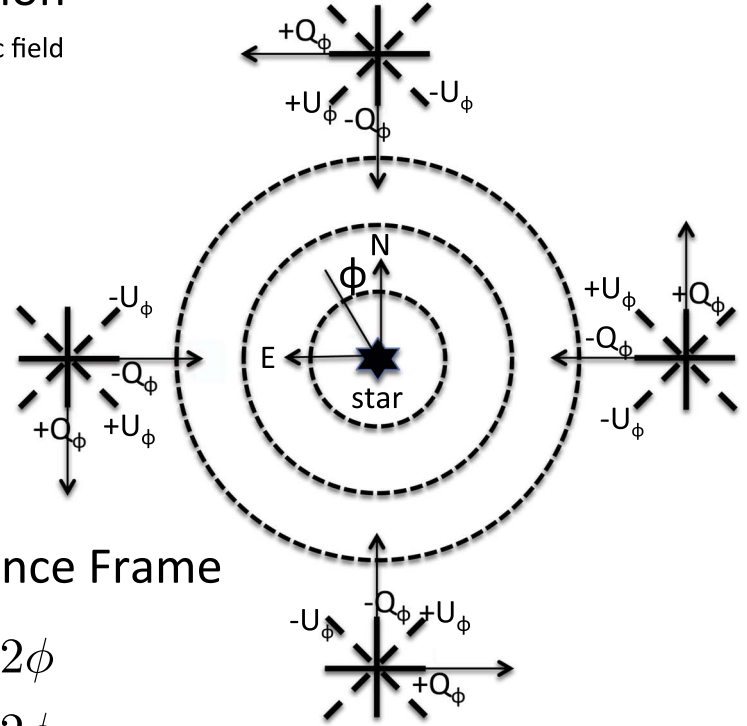
¹⁵ <http://ascl.net/1411.018>

¹⁶ <http://ascl.net/1208.019>

IAU Stokes Q,U Convention



Plane of electric field



Definition of Q_ϕ, U_ϕ Reference Frame

$$Q_\phi = -Q \cos 2\phi - U \sin 2\phi$$

$$U_\phi = +Q \sin 2\phi - U \cos 2\phi$$

Figure 15. Definitions of the Stokes Q , U , and Q_ϕ , U_ϕ used in this paper.

1. Consistent with IAU recommendations for Q , U position angles
2. Yields positive Q_ϕ for cases when E-field polarization angle at a given pixel is perpendicular to the vector connecting the pixel and the star's location
3. Results for Q_ϕ , U_ϕ maps (including the sign \pm) agree with previously published polarization imaging by GPI, NACO, and SPHERE groups (despite confusing or incomplete descriptions of conventions contained therein).

Appendix B

Hubble Space Telescope Analysis

The *Hubble Space Telescope* observed HD 34700A on 1998 September 17 using NICMOS/NIC2-CORON (PI: Bradford Smith). Sterzik et al. (2005) already inspected these data to

show HD 34700B and HD 34700C were co-moving with HD 34700A. We were interested in data taken with the wide F110W filter (0.8–1.4 μm); to look for evidence of the scattered light ring, we imaged with GPI at a similar wavelength. Figure 16 shows the difference between two images taken at two different telescope roll angles. In this difference image, the PSF structures should cancel but leave positive/negative imprints of circumstellar structure or companions. One can see there is complex residual flux around the coronagraphic spot and what appears to be a newly discovered companion HD 34700D, a possible fifth member of the HD 34700 system. A preliminary analysis indicates that HD 34700D is located at distance $6''.45$ (projected 2300 au) along PA $-60^\circ.9$ with $\text{mag}_{F110W} = 18.6$. This flux density corresponds to an absolute magnitude $M_{F110W} = 10.9$, leading to a mass estimate of 12–15 M_J (Chabrier et al. 2000, assuming $t = 5$ Myr), a borderline planet/brown dwarf object assuming it is physically

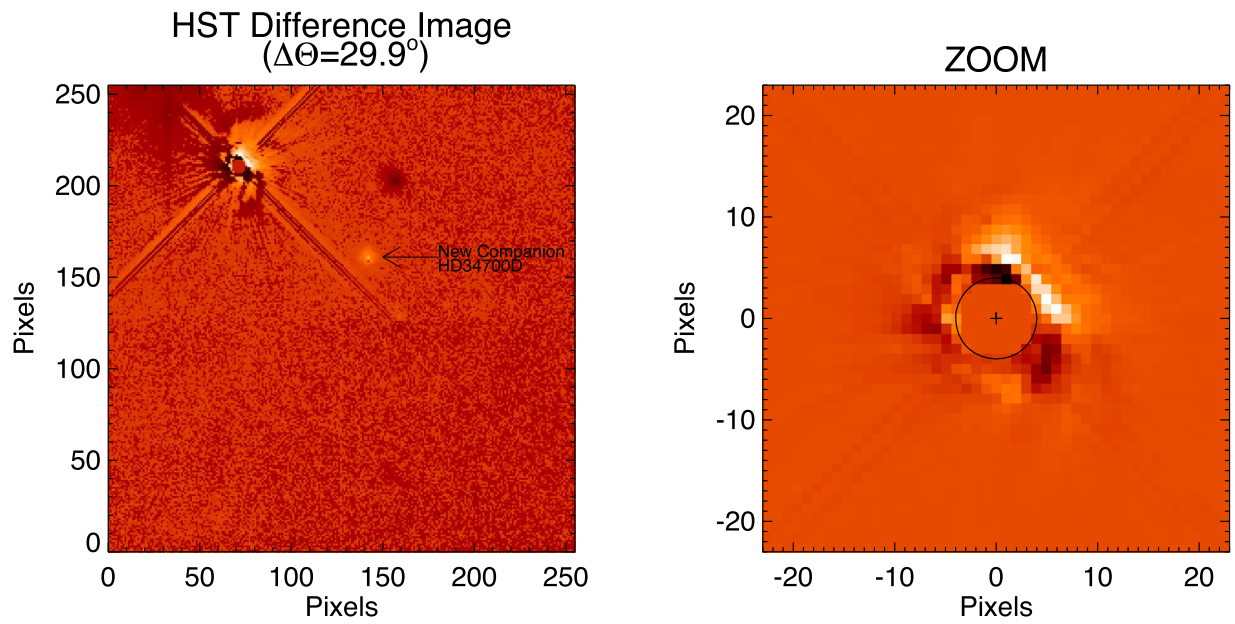


Figure 16. Difference of two *HST*/NICMOS (filter F110W) images with telescope roll angles changed by 29.9^{circ} . (left panel) We see the full image here with the location of the newly discovered HD 34700D marked (separation $6''.45$ along PA $-60^\circ.9$). The color table is proportional to intensity $|I|^{1/2}$ while maintaining signs to show low contrast features. (Right panel) Here is a zoom-up of the inner $3''.5$ around the coronagraphic spot (marked by the black circle) shown with a linear intensity color table. Pixel scale is 75 mas/pixel .

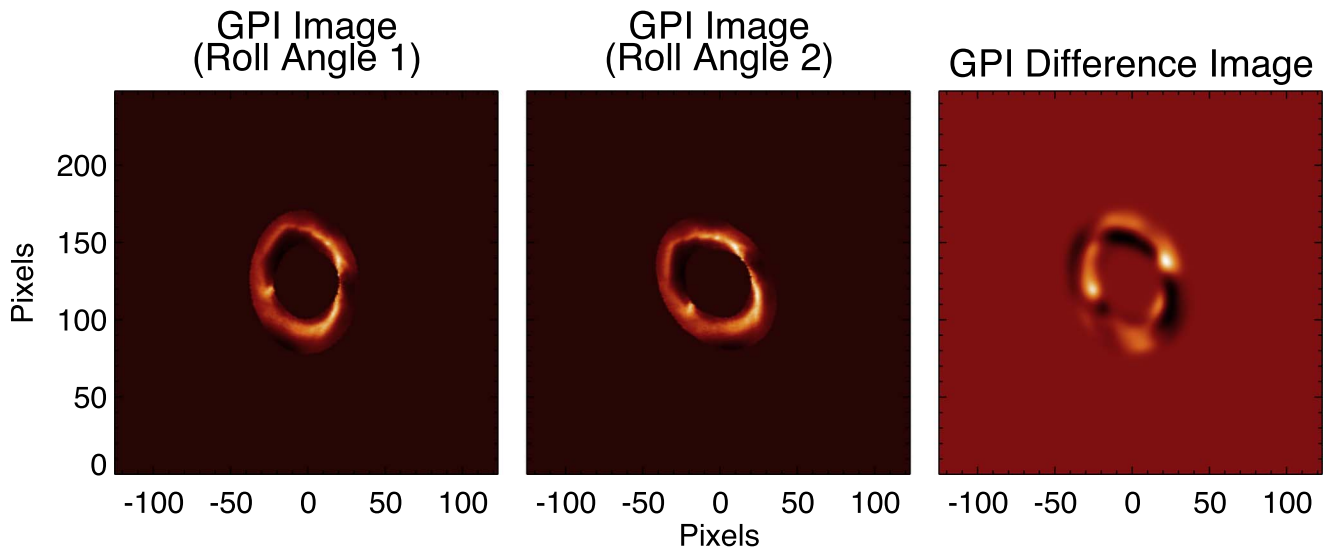


Figure 17. GPI total intensity image at the two roll angles observed by *HST*. The right-most panel shows the difference image and can be directly compared to the right panel in Figure 16. A mask is applied to only show regions where our total intensity image is valid (within 25% of the elliptical ring structure). Pixel scale is 14.14 mas/pixel , and the field of view is $\sim 3''.5$.

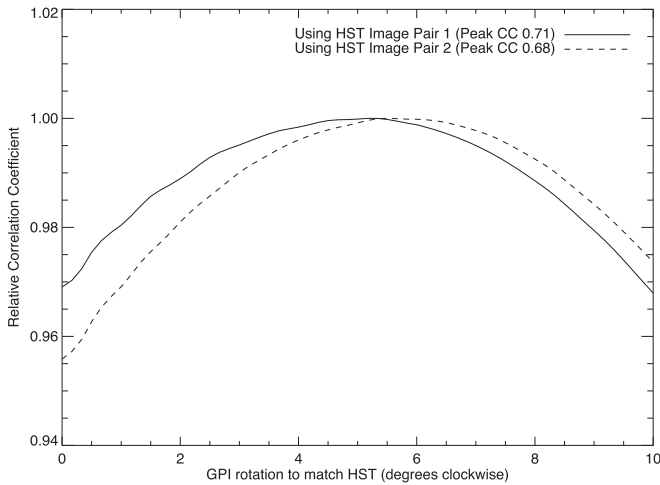


Figure 18. GPI correlation analysis for two independent *HST* image pairs. The GPI difference image agrees better with the *HST* image if we rotate the GPI image by $5^{\circ}75 \pm 0^{\circ}25$, suggesting the HD 34700A disk is rotating counterclockwise with an orbital period of ~ 1200 yr at the radial location of the ring.

associated with HD 34700ABC. New *HST* data was recently obtained that might allow the proper motion to be determined, although these data are still protected at the moment.

In order to understand the residual flux around the coronagraphic spot, we simulated the *HST* roll angle differences using our GPI total intensity image. Figure 17 shows the GPI image at both roll angles used by *HST* and the resulting difference. The correlation between the *HST* difference image is clear, although some differences are apparent. After a visual inspection, we suspected a very slight rotation between the *HST* and GPI difference images, and we explored this using a correlation analysis over (x, y) shifts and image rotation. We also varied the size of the occulting mask, smoothing kernel to degrade the GPI resolution to match *HST*, and also tried using both sets of *HST* F110W difference images in the archive. No matter how we changed the details of the correlation analysis, we found the correlation was best ($\sim 71\%$) when rotating the GPI image clockwise by $\sim 5^{\circ}75$. For a

300 mas coronagraphic spot mask and a GPI smoothing FWHM of 70 mas, Figure 18 shows the correlation coefficient for a range of rotation angles (optimizing the translation match for each candidate rotation angle) with a peak at $5^{\circ}5$ for data set 1 and with a peak at $6^{\circ}0$ for data set 2. Since uncertainties here are strongly dominated by systematics and not random errors associated with photon noise, we have used these two independent data sets to estimate our optimal rotation angle and associated error: $5^{\circ}75 \pm 0^{\circ}25$. Our correlation analyses also allow us to estimate that the GPI flux is ~ 3.3 higher than the *HST* data; while the 19-year time difference and different passbands make a precise cross-calibration difficult, this discrepancy supports our conclusion that the GPI photometry is poorly calibrated in terms of the absolute flux level.

While there is not a large difference in the correlation coefficient between no rotation (68.5%) and with $5^{\circ}5$ rotation (71.2%), the difference is persistent for multiple data sets and a wide range of methodology details. If taken seriously, this would mean the disk is rotating counterclockwise, consistent with the winding of the spiral arms, with an orbital period of 1200 ± 50 yr. This is in excellent agreement with the expected Keplerian orbital period of 1160 yr for our disk model (dust ring at 175 au around a $4 M_{\odot}$ central mass).

As a check, we also performed a more complicated analysis where we first deprojected the ring into a face-on view, applied rotation, then re-projected the result—this would separate out rotation of the ellipse itself on-sky (not expected) from rotation of structures along the ellipse (expected from orbital motion). The highest correlation from this analysis was for $8^{\circ}3$ rotation, somewhat higher than from our first approach. Again, we urge caution in interpreting this rotation result because it is possible that artifacts from diffraction near the coronagraphic spot may accidentally mimic the effects of a tiny rotation, but we report the results of our work anyway.

Appendix C Additional Hydrodynamic Models

The purpose of this appendix section is to make it clear that (1) it is not the circumplanetary disk (CPD) itself creating the

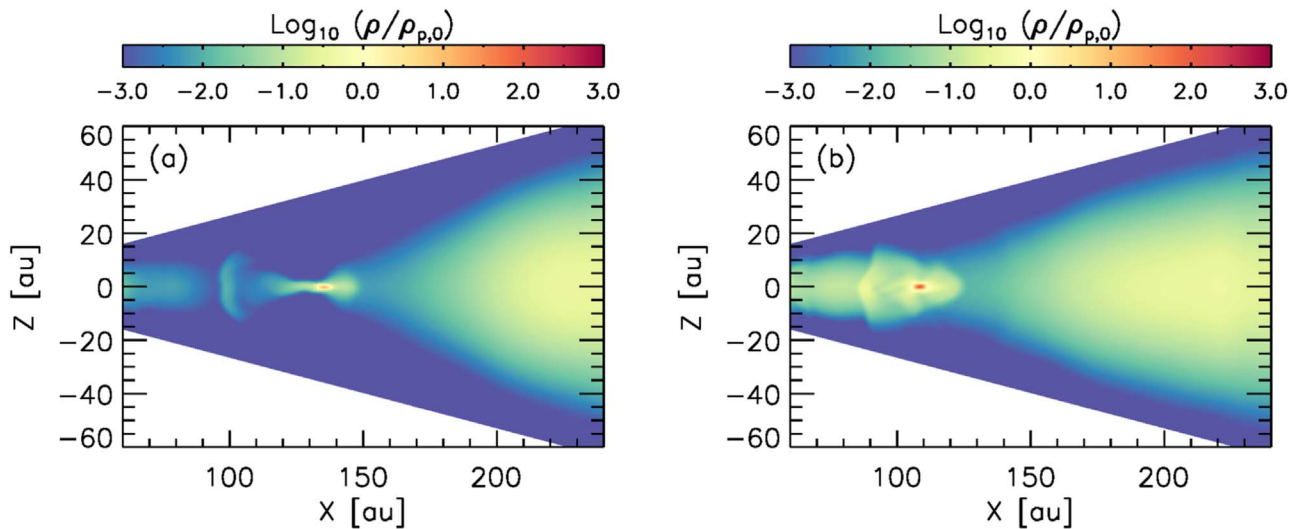


Figure 19. Same as Figure 14 but with (a) a $50M_{\text{Jup}}$ planet having zero orbital eccentricity, and (b) a $10M_{\text{Jup}}$ planet having 0.2 orbital eccentricity. Compared with the fiducial model presented in Figure 14, these models suggest that a large planetary mass or a non-zero eccentricity alone is not sufficient to create optically thick three-dimensional flows capable of casting shadow onto the outer disk.

shadow shown in Figure 14, but rather the flow around/onto the CPD; and (2) a hypothetical planet has to have sufficiently large mass and a non-zero eccentricity to produce such flows. In Figure 19 we present vertical density distributions from two additional hydrodynamic models. Figure 19(a) demonstrates that a $50 M_J$ planet with a circular orbit has a CPD that remains geometrically thin. The planet does not produce vertical flows around it, unlike our fiducial model presented in Section 5. As the CPD is geometrically thin, it does not cast a significant shadow onto the outer disk. Figure 19(b) presents that a $10 M_J$ planet with 0.2 orbital eccentricity can produce some vertical flows around the CPD. Compared with Figure 19(a), this suggests that vertical circumplanetary flows may require a non-zero orbital eccentricity to develop. In addition, comparing with Figure 14(c) we find that the strength and vertical extent

of circumplanetary flows is dependent on planet mass: a larger planet mass results in stronger and more vertically extended flows. When post-processed with radiative transfer calculations, however, this model fails to reproduce the observed discontinuity in the outer ring, presumably because the density and/or vertical extent of the circumplanetary flows is not sufficient.

Appendix D Additional Figures

In order to aid other researchers in comparing our results to images taken at other wavelengths, we provide reference figures (see Figures 20 and 21) here of our polarized intensity Q_ϕ surface-brightness maps without contours or distracting labels.

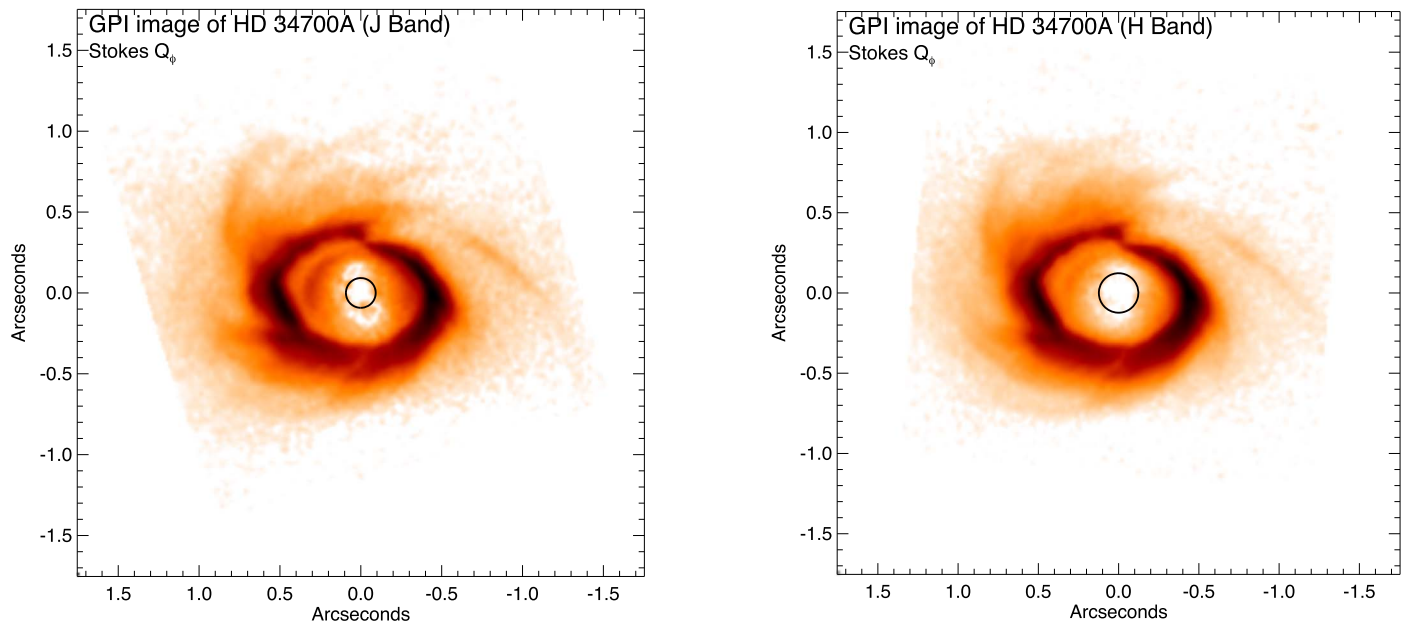


Figure 20. Polarized intensity Q_ϕ images of HD 34700A in J band (left panel) and in H band (right panel). We present these images without contours to aid researchers in comparing our results with multi-wavelength imaging data from other facilities—see Figure 2 for full details on the color table. The circle marks the location and size of the coronagraphic spot used for the H -band observations.

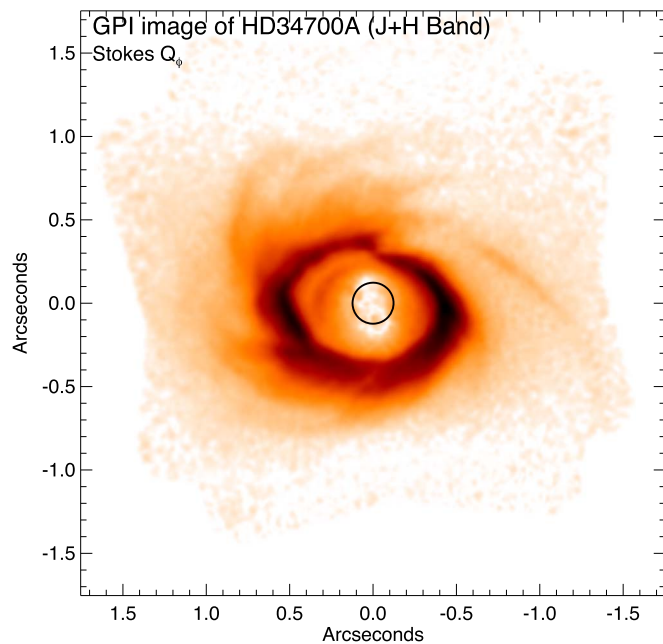


Figure 21. We present a combined J -band and H -band polarized intensity image to achieve best signal-to-noise ratio for identifying features in the disk. These images are shown without contours to aid researchers in comparing our results with multi-wavelength imaging data from other facilities. The circle marks the location and size of the coronagraphic spot used for the H -band observations.

ORCID iDs

John D. Monnier <https://orcid.org/0000-0002-3380-3307>
 Tim J. Harries <https://orcid.org/0000-0001-8228-9503>
 Jaehan Bae <https://orcid.org/0000-0001-7258-770X>
 Benjamin R. Setterholm <https://orcid.org/0000-0001-5980-0246>
 Alicia Aarnio <https://orcid.org/0000-0002-1327-9659>

Fred C. Adams <https://orcid.org/0000-0002-8167-1767>
 Sean Andrews <https://orcid.org/0000-0003-2253-2270>
 Nuria Calvet <https://orcid.org/0000-0002-3950-5386>
 Catherine Espaillat <https://orcid.org/0000-0001-9227-5949>
 Lee Hartmann <https://orcid.org/0000-0003-1430-8519>
 Stefan Kraus <https://orcid.org/0000-0001-6017-8773>
 Melissa McClure <https://orcid.org/0000-0003-1878-327X>
 Chris Miller <https://orcid.org/0000-0002-1365-084>
 Rebecca Oppenheimer <https://orcid.org/0000-0001-7130-7681>
 David Wilner <https://orcid.org/0000-0003-1526-7587>
 Zhaohuan Zhu <https://orcid.org/0000-0003-3616-6822>

References

- Avenhaus, H., Quanz, S. P., Garufi, A., et al. 2018, *ApJ*, 863, 44
 Avenhaus, H., Quanz, S. P., Schmid, H. M., et al. 2014, *ApJ*, 781, 87
 Avenhaus, H., Quanz, S. P., Schmid, H. M., et al. 2017, *AJ*, 154, 33
 Bae, J., & Zhu, Z. 2018a, *ApJ*, 859, 119
 Bae, J., & Zhu, Z. 2018b, *ApJ*, 859, 118
 Bae, J., Zhu, Z., & Hartmann, L. 2017, *ApJ*, 850, 201
 Benisty, M., Juhasz, A., Boccaletti, A., et al. 2015, *A&A*, 578, L6
 Benisty, M., Stolker, T., Pohl, A., et al. 2017, *A&A*, 597, A42
 Benítez-Llambay, P., & Masset, F. S. 2016, *ApJS*, 223, 11
 Bhatt, H. C., & Manoj, P. 2000, *A&A*, 362, 978
 Birmstiel, T., Dullemond, C. P., & Brauer, F. 2010, *A&A*, 513, A79
 Boss, A. P. 1997, *Sci*, 276, 1836
 Canovas, H., Ménard, F., de Boer, J., et al. 2015, *A&A*, 582, L7
 Chabrier, G., Baraffe, I., Allard, F., & Hauschildt, P. 2000, *ApJ*, 542, 464
 Cossins, P., Lodato, G., & Clarke, C. J. 2009, *MNRAS*, 393, 1157
 De Rosa, R. J., Nielsen, E. L., Blunt, S. C., et al. 2015, *ApJL*, 814, L3
 Dong, R., Fung, J., & Chiang, E. 2016a, *ApJ*, 826, 75
 Dong, R., Hall, C., Rice, K., & Chiang, E. 2015, *ApJL*, 812, 32
 Dong, R., Zhu, Z., Fung, J., et al. 2016b, *ApJL*, 816, L12
 Draine, B. T., & Lee, H. M. 1984, *ApJ*, 285, 89
 Fedele, D., Tazzari, M., Booth, R., et al. 2018, *A&A*, 610, A24
 Forgan, D. H., Ramón-Fox, F. G., & Bonnell, I. A. 2018, *MNRAS*, 476, 2384
 Fujii, T., Nakada, Y., & Parthasarathy, M. 2002, *A&A*, 385, 884
 Fung, J., & Dong, R. 2015, *ApJL*, 815, L21
 Gaia Collaboration, Brown, A. G. A., Vallenari, A., et al. 2018, *A&A*, 616, A1
 Garufi, A., Benisty, M., Stolker, T., et al. 2017, *Msngr*, 169, 32
 Garufi, A., Quanz, S. P., Schmid, H. M., et al. 2014, *A&A*, 568, A40

- Goldreich, P., & Tremaine, S. 1980, *ApJ*, 241, 425
- Hamaker, J. P., & Bregman, J. D. 1996, *A&AS*, 117, 161
- Harries, T. J. 2000, *MNRAS*, 315, 722
- Harries, T. J. 2011, *MNRAS*, 416, 1500
- Harries, T. J., Monnier, J. D., Symington, N. H., & Kurosawa, R. 2004, *MNRAS*, 350, 565
- Huang, J., Andrews, S. M., Cleeves, L. I., et al. 2018, *ApJ*, 852, 122
- Hung, L.-W., Bruzzone, S., Millar-Blanchaer, M. A., et al. 2016, *Proc. SPIE*, 9908, 99083A
- IAU 1974, IAUTB, 15, 166
- Johansen, A., Oishi, J. S., Mac Low, M.-M., et al. 2007, *Natur*, 448, 1022
- Juhász, A., & Rosotti, G. P. 2018, *MNRAS*, 474, L32
- Kenyon, S. J., & Hartmann, L. 1987, *ApJ*, 323, 714
- Konopacky, Q. M., Thomas, S. J., Macintosh, B. A., et al. 2014, *Proc. SPIE*, 9147, 914784
- Lucy, L. B. 1999, *A&A*, 344, 282
- Macintosh, B., Graham, J. R., Ingraham, P., et al. 2014, *PNAS*, 111, 12661
- Macintosh, B. A., Graham, J. R., Palmer, D. W., et al. 2008, *Proc. SPIE*, 7015, 701518
- Masset, F. 2000, *A&AS*, 141, 165
- Mathis, J. S., Rumpl, W., & Nordsieck, K. H. 1977, *ApJ*, 217, 425
- Mendigutía, I., Mora, A., Montesinos, B., et al. 2012, *A&A*, 543, A59
- Millar-Blanchaer, M. A., Perrin, M. D., Hung, L.-W., et al. 2016, *Proc. SPIE*, 9908, 990836
- Monnier, J. D., Harries, T. J., Aarnio, A., et al. 2017, *ApJ*, 838, 20
- Mora, A., Merín, B., Solano, E., et al. 2001, *A&A*, 378, 116
- Oppenheimer, B. R., Brenner, D., Hinkley, S., et al. 2008, *ApJ*, 679, 1574
- Oudmaijer, R. D., Palacios, J., Eiroa, C., et al. 2001, *A&A*, 379, 564
- Perrin, M. D., Duchene, G., Millar-Blanchaer, M., et al. 2015, *ApJ*, 799, 182
- Perrin, M. D., Maire, J., Ingraham, P., et al. 2014, *Proc. SPIE*, 9147, 91473J
- Pierens, A., & Nelson, R. P. 2018, *MNRAS*, 477, 2547
- Pinte, C., Harries, T. J., Min, M., et al. 2009, *A&A*, 498, 967
- Pollack, J. B., Hubickyj, O., Bodenheimer, P., et al. 1996, *Icar*, 124, 62
- Poyneer, L. A., Palmer, D. W., Macintosh, B., et al. 2016, *ApOpt*, 55, 323
- Price, D. J., Cuello, N., Pinte, C., et al. 2018, *MNRAS*, 477, 1270
- Rapson, V. A., Kastner, J. H., Millar-Blanchaer, M. A., & Dong, R. 2015, *ApJL*, 815, L26
- Robitaille, T. P. 2011, *A&A*, 536, A79
- Schmid, H. M., Joos, F., & Tschan, D. 2006, *A&A*, 452, 657
- Seok, J. Y., & Li, A. 2015, *ApJ*, 809, 22
- Siess, L., Dufour, E., & Forestini, M. 2000, *A&A*, 358, 593
- Skrutskie, M. F., Cutri, R. M., Stiening, R., et al. 2006, *AJ*, 131, 1163
- Sterzik, M. F., Melo, C. H. F., Tokovinin, A. A., & van der Bliik, N. 2005, *A&A*, 434, 671
- Sylvester, R. J., Skinner, C. J., Barlow, M. J., & Mannings, V. 1996, *MNRAS*, 279, 915
- Tanaka, H., Takeuchi, T., & Ward, W. R. 2002, *ApJ*, 565, 1257
- Torres, G. 2004, *AJ*, 127, 1187
- Wang, J. J., Rajan, A., Graham, J. R., et al. 2014, *Proc. SPIE*, 9147, 914755
- Wenger, M., Ochsenein, F., Egret, D., et al. 2000, *A&AS*, 143, 9
- Wolff, S. G., Perrin, M., Millar-Blanchaer, M. A., et al. 2016, *ApJL*, 818, L15
- Wood, K., Whitney, B. A., Robitaille, T., & Draine, B. T. 2008, *ApJ*, 688, 1118
- Zhu, Z., Dong, R., Stone, J. M., & Rafikov, R. R. 2015, *ApJ*, 813, 88